

# CERIA DOPED LEAD ZIRCONATE TITANATE CERAMICS

A Thesis Submitted  
in Partial Fulfilment of the Requirements  
for the Degree of

MASTER OF TECHNOLOGY

*by*

SANJAY KUMAR NAG

*to the*

Interdisciplinary Programme in Materials Science  
INDIAN INSTITUTE OF TECHNOLOGY, KANPUR

JULY, 1990

18 SEP 1990

CENTRAL LIBRARY  
I. I. T., KANDUR

---

Acc. No. **A.108886**

Dedicated  
to  
My Parents

## CERTIFICATE

This is to certify that this work on "CERIA DOPED LEAD ZIRCONATE TITANATE CERAMICS" by Sanjay Kumar Nag has been carried out under my supervision and that this has not been submitted elsewhere for a degree.

July, 1990.

D.C. Agarwal  
Professor  
Materials Science Programme  
Indian Institute of Technology  
Kanpur



## ACKNOWLEDGEMENTS

I wish to express my profound sense of gratitude to Prof. D.C. Agrawal for his excellent guidance and inspiration in every step of my work.

I am extremely grateful to Dr. K.N. Rai for allowing me to have free access to all the facilities for piezoelectric measurements.

I sincerely appreciate the companionship of all my friends Bhangui, Sanjay, Murli, Kripa Shankar, Promod, Ramani, Ajai Srinivas, and Mr. V.V. Mishra.

Special thanks are due to Ms. Shuli Gupta, Santanu, Sambi and Subhashish for all sorts of help, cooperation, and encouragement in different stages of my work.

I also express my heartfelt appreciation of the help and cooperation by all the staff members of ACMS.

Special thanks are due to Mr. P.K. Pal, Mr. B.K. Jain, Mr. B. Sharma and Umasankarji.

Thanks are also due to Mr. U.S. Mishra for his prompt and excellent typing of this manuscript.

**Sanjay Kumar Nag**

## CONTENTS

	Page No.
LIST OF TABLES	v
LIST OF FIGURES	vii
ABSTRACT	x
CHAPTER 1 INTRODUCTION	
1.1 Piezoelectricity	1
1.2 Piezoelectric Constants	2
1.3 Piezoelectricity In Ceramics	8
1.4 PZT Piezoelectric Ceramics	13
1.5 Processing Parameters of PZT Ceramics	19
1.6 Doping Effect to PZT Ceramics	26
1.7 Present Work	34
CHAPTER 2 SAMPLE PREPARATION AND CHARACTERISATION	
2.1 Sample Preparation	35
2.1.1 Raw Materials	35
2.1.2 Preparation of Atmosphere Powder	35
2.1.3 Preparation of PZT Compositions	36
2.2 Phase Analysis	40
2.3 Measurement of Sintered Density	43
2.4 Measurement of Piezoelectric Properties	43
2.4.1 Poling	43
2.4.2 Sample Size and Shape	45
2.4.3 Poling Process	46
2.4.4 Measurement Techniques	48
2.5 Measurement of Mechanical Properties	57
2.5.1 Vickers Hardness	57
2.5.2 Modulus of Rupture	58
2.5.3 Youngs Modulus	61
2.5.4 Fracture Toughness	62
2.6 Microstructure Analysis	63
CHAPTER 3 RESULTS AND DISCUSSION	
3.1 Phase Analysis	64
3.2 Sintered Density	70
3.3 Piezoelectric Properties	72
3.4 Mechanical Properties	84
3.4.1 Vickers Hardness	85
3.4.2 Modulus of Rupture	87
3.4.3 Youngs Modulus	87
3.4.4 Fracture Toughness	88

3.5	Microstructure Analysis	93
CHAPTER 4	CONCLUSION AND FURTHER SCOPE OF RESEARCH	97
	REFERENCES	99
	APPENDIX	107

LIST OF TABLES

1.1	Some possible arrangements for the substitution of A and B sites in the perovskite structure. The dopants which go to a particular site are also given	28
1.2	Compositions and properties	33
2.1	Details of chemicals used	35
2.2	Chemical compositions of PZT doped with ceria	36
2.3	Calcining schedule	37
2.4	Sintering schedule	39
2.5	Conditions for operation of X-ray Diffractometer	40
3.1	Lattice parameters for Tetragonal phase in PZT	69
3.2	Density of ceria doped PZT ceramics	71
3.3	Range of resonant and antiresonant frequencies	72
3.4	Range of capacitance of the PZT samples at 100 KHz frequency	74
3.5	Dielectric constant of ceria doped PZT ceramics at 100 KHz frequency	75
3.6	Elastic compliance of ceria doped PZT ceramics	75
3.7	Electrochemical coupling coefficients of ceria doped PZT ceramics	76
3.8	Voltage coefficient of ceria doped PZT ceramics	76
3.9	Strain coefficients of ceria doped PZT ceramics	77

3.10 Vickers Hardness of ceria doped PZT ceramics	85
3.11 MOR of ceria doped PZT ceramics	87
3.12 Youngs modulus of ceria doped PZT ceramics	88
3.13 Fracture toughness of ceria doped PZT ceramics.	89

LIST OF FIGURES

1.1	Notation of axes for poled ceramic element	6
1.2	Interrelationship of piezoelectrics and subgroups on the basis of internal crystal symmetry	10
1.3	The perovskite structure as typified by $\text{BaTiO}_3$ above its Curie temperature	12
1.4	Ions position in tetragonal $\text{BaTiO}_3$	12
1.5	Distortions in (a) the $\text{TiO}_6$ and (b) the $\text{PbO}_{12}$ coordination polyhedra of tetragonal $\text{PbTiO}_3$ . The two crystallographically distinct oxygens are labelled $O_1$ and $O_{11}$ .	14
1.6	Unit cell distortion at room temperature for the $\text{PbTiO}_3$ - $\text{PbZrO}_3$ system.	16
1.7	$\text{PbTiO}_3$ - $\text{PbZrO}_3$ sub-solids phase diagram	16
1.8	Flow sheet for solid state processing of PZT ceramics.	21
1.9	Composition-temperature and composition - activity of $\text{PbO-TiO}_2$ and $\text{PbO-ZrO}_2$ system.	24
1.10	Effect of calcination temperature on the density of end products	27
1.11	Effect of sintering soak time on the density of end products	27
2.1	(a) Schematic diagram of crucible arrangement during calcination	30

2.1	(b) Schematic diagram of crucible arrangement during sintering.	38
2.2	Schematic diagram of poling fixture.	47
2.3	Transmission network for determination of $f_r$ and $f_a$ of piezoelectric ceramic vibrator	50
2.4	(a) Equivalent circuit of a piezoelectric body.	51
2.4	(b) Reactance of piezoelectric resonator.	51
2.5	Planer coupling factor of thin disk.	53
2.6	Four point bending fixture.	59
2.7	(a) Specimen configuration for MOR and Youngs Modulus test.	60
2.7	(b) Specimen configuration for $K_{IC}$ test.	60
3.1	Slow scan XRD pattern of PZT ( $X = 0.535$ )	65
3.2	Slow scan XRD-pattern of calcined PZT powders with $CeO_2$ varying from 0-5.0 mole%.	66
3.3	Details of slow scan XRD-patterns of sintered samples.	67
3.4	Free $CeO_2$ is present only at the highest $CeO_2$ content at 5 mole%.	68
3.5	Variation of density with concentration of ceria.	71
3.6	Variation of reactance with frequency.	73
3.7	Variation of free relative dielectric constant with concentration of ceria.	79
3.8	Variation of elastic compliance with concentration of ceria.	80

3.9	Variation of coupling coefficient with concentration of ceria.	81
3.10	Variation of voltage coefficient with concentration of ceria.	82
3.11	Variation of strain coefficient with concentration of ceria.	83
3.12	Variation of Vickers Hardness with concentration of ceria.	86
3.13	Variation of Youngs modulus, Modulus of Rupture and Fracture toughness with concentration of ceria.	90



ABSTRACT

Lead Zirconate Titanate (PZT) ceramics with composition at the morphotropic phase boundary have been doped with 0, 0.1, 1.0, 2.0 and 5.0 mole %  $\text{CeO}_2$ .

The ceramic samples have been synthesized by calcining the powder mixture at  $960^\circ\text{C}$  for 4 hrs and then sintering at  $1200^\circ\text{C}$  for 4 hrs in an atmosphere of PZ + 5 wt% PbO atmosphere powder. The compositions have been studied with regard to, i) phase analysis, ii) density, iii) piezoelectric properties, iv) mechanical properties including Vickers Hardness, Modulus of Rupture (MOR), Youngs Modulus and fracture toughness ( $K_{IC}$ ) and v) microstructures.

Analysis of experimental results shows that the tetragonal and rhombohedral phases coexist upto 0.1 mole %  $\text{CeO}_2$  beyond which only the tetragonal phase is present. c/a ratio of the tetragonal phase also gradually increases with  $\text{CeO}_2$  concentration. Maximum piezoelectric properties are obtained at 0.1 mole %  $\text{CeO}_2$  concentration.

Density is minimum at 1.0 mole %  $\text{CeO}_2$ . Good correlation between density and MOR is observed. There is rise in  $K_{IC}$  after a minimum. This is correlated with the appearance of  $\text{CeO}_2$  particles at the grain boundaries.

Microstructural analysis show gradual rise in the grain size with increasing concentration of  $\text{CeO}_2$ .

## CHAPTER 1

### INTRODUCTION

#### 1.1 Piezoelectricity:

Piezoelectricity was discovered in 1880 by Pierre and Jacques Curie during their systematic investigation of the effect of pressure on the generation of electrical charge by crystals such as quartz, zincblend, tourmaline and rochelle salt. The term 'Piezoelectricity' (pressure electricity) was first suggested by W. Hankel in 1881. Cady [1] defines piezoelectricity as "electrical polarization produced by mechanical strain in crystals belonging to certain classes, the polarization being proportional to the strain and changing sign with it". Piezoelectric effect is categorized in two classes, viz. i) Direct piezoelectric effect and ii) Converse or Inverse piezoelectric effect.

#### Direct Piezoelectric Effect:

This is characterised by the generation of electrical charge (polarization) under mechanical stress.

#### Converse Piezoelectric Effect:

It is associated with the mechanical movement generated by the application of an electric field.

Both these effects are manifestation of the same fundamental property of the crystal and therefore, belong to the reversible physical phenomena.

Electric field and polarization are vectors while mechanical stress and strain are described by tensors which do not have the one way directional characteristics. For piezoelectric interactions to exist, it is therefore necessary that certain axes of the medium intrinsically possess polarity. A body or any one of its physical properties may be symmetrical with respect to i) a point, ii) a line, iii) a plane or iv) any combination of these. If symmetrical with respect to a 'point', the body is 'central symmetric' and can not possess polar properties. Thus 'non-centrosymmetry' is the essential condition for piezoelectricity with only one exception. 21 out of the 32 crystal classes are non-centrosymmetric. 20 out of 21 crystal classes show piezoelectricity. The single exception is (432) class of crystals. Though this (432) class of crystal is noncentrosymmetric it has other symmetry elements that combine to exclude the piezoelectric property.

## 1.2 Piezoelectric Constants:

Ordinary solids under a stress  $T$  show a proportional strain  $S$  given by  $T = Y.S$ . But piezoelectricity implies additional creation of electric charge. The equations of state that describe a piezoelectric body in regard to its electric and elastic properties are, in their general form, as follows:

$$D = d.T + \sum^T E \quad (\text{Direct piezoelectric effect})$$

$$\text{and} \quad S = s.T + d.E \quad (\text{Converse piezoelectric effect})$$

where,  $D$  = Dielectric displacement

T = Stress

S = Strain

E = Electric field

d = a piezoelectric coefficient

s = The material compliance (inverse of stiffness)

$\epsilon$  = Dielectric constant.

For both the direct and the converse effects, the 'd' coefficient is the proportionality constant between displacement and stress, or strain and electric field according to the relationships

$$d = \frac{D}{T} = \frac{S}{E} \text{ (meters/volt. or Coulomb/Newton)}$$

and is known as charge or strain coefficient.

Another frequently used piezoelectric constant is 'g' which gives the field produced by stress and is known as piezoelectric voltage coefficient,

$$g = \frac{E}{T} = \frac{S}{D} \cdot \left[ \frac{\text{Volt/meter}}{\text{Newton/sq.meter}} = \frac{\text{Volt-meter}}{\text{Newton}} \right]$$

Rigorous development of these relationship may be found elsewhere [2,3]. Jaffe and Berlincourt [3] defined the piezoelectric constants as partial derivatives evaluated at constant stress (subscript T), constant field (subscript E), constant displacement (subscript D) or constant strain (subscript S). These boundary conditions can be thought as "free", "short circuit", "open circuit" and "clamped" respectively. The definitions are

$$d = \left( \frac{\partial S}{\partial E} \right)_T = \left( \frac{\partial D}{\partial T} \right)_E$$

$$g = \left( - \frac{\partial E}{\partial T} \right)_D = \left( \frac{\partial S}{\partial D} \right)_T$$

These are derived from the equations of state of a solid body. For ceramics and crystals, the elastic, dielectric and piezoelectric constants may differ along different axes. For this reason they are expressed in tensor form [3].

The best single measurement of the strength of a piezoelectric effect is the electromechanical coupling factor  $k$ . When an electric field is applied it measures the fraction of the electrical energy converted to mechanical energy (or vice versa when a crystal or ceramic is stressed).

The actual relationship is in terms of  $k^2$ .

$$k^2 = \frac{\text{electrical energy converted to mechanical energy}}{\text{input electrical energy}}$$

or,

$$k^2 = \frac{\text{mechanical energy converted to electrical energy}}{\text{input mechanical energy}}$$

As the conversion is always incomplete the value of  $k$  is always  $< 1$ . Typical values of  $k$  are 0.1 for quartz, 0.4 for barium titanate ceramic, 0.3~0.7 for  $\text{Pb}(\text{Zr}_{1-x}\text{Ti}_x)_3\text{O}_{10}$ ,  $0 < x < 1$ ,

and as high as 0.9 for Rochelle salt at its Curie point (24 °C).

Dielectric constant is another important property of these materials. The relative dielectric constant,  $K$ , or  $\epsilon/\epsilon_0$

is the ratio between the charge stored on an electrode of this material brought to a given voltage and the charge stored on a set of identical electrodes separated by vacuum. The relative dielectric constant is dimensionless quantity. It depends on the orientation of grains of piezoelectric materials and differs widely when measured parallel or perpendicular to the polar axis [1]. The dielectric constant when measured at constant stress is called 'free' dielectric constant denoted by superscript 'T' and when measured under constant strain is known as 'clamped' dielectric constant denoted by superscript 'S'. The free and clamped dielectric constant may differ greatly for strong piezoelectric materials. The relation between the two is

$$\frac{S}{K} = \frac{T}{K} \left(1 - \frac{k_p^2}{1}\right)$$

where  $k_p$  is electromechanical coupling coefficient (planer).

A convenient method [4] of uniquely specifying all these directional properties is to use subscripts which defines orientation direction as described in figure 1.1. The '3' direction is usually taken as poling (polar) axis and '1' and '2' directions are orthogonal axes to '3'. Shear effects are indicated by the subscripts '4', '5' and '6'. Coefficients that relate two variables (e.g., the 'd' constant) are indicated with two subscripts, the first of which refers to the electrical direction (electric field or dielectric displacement) and the

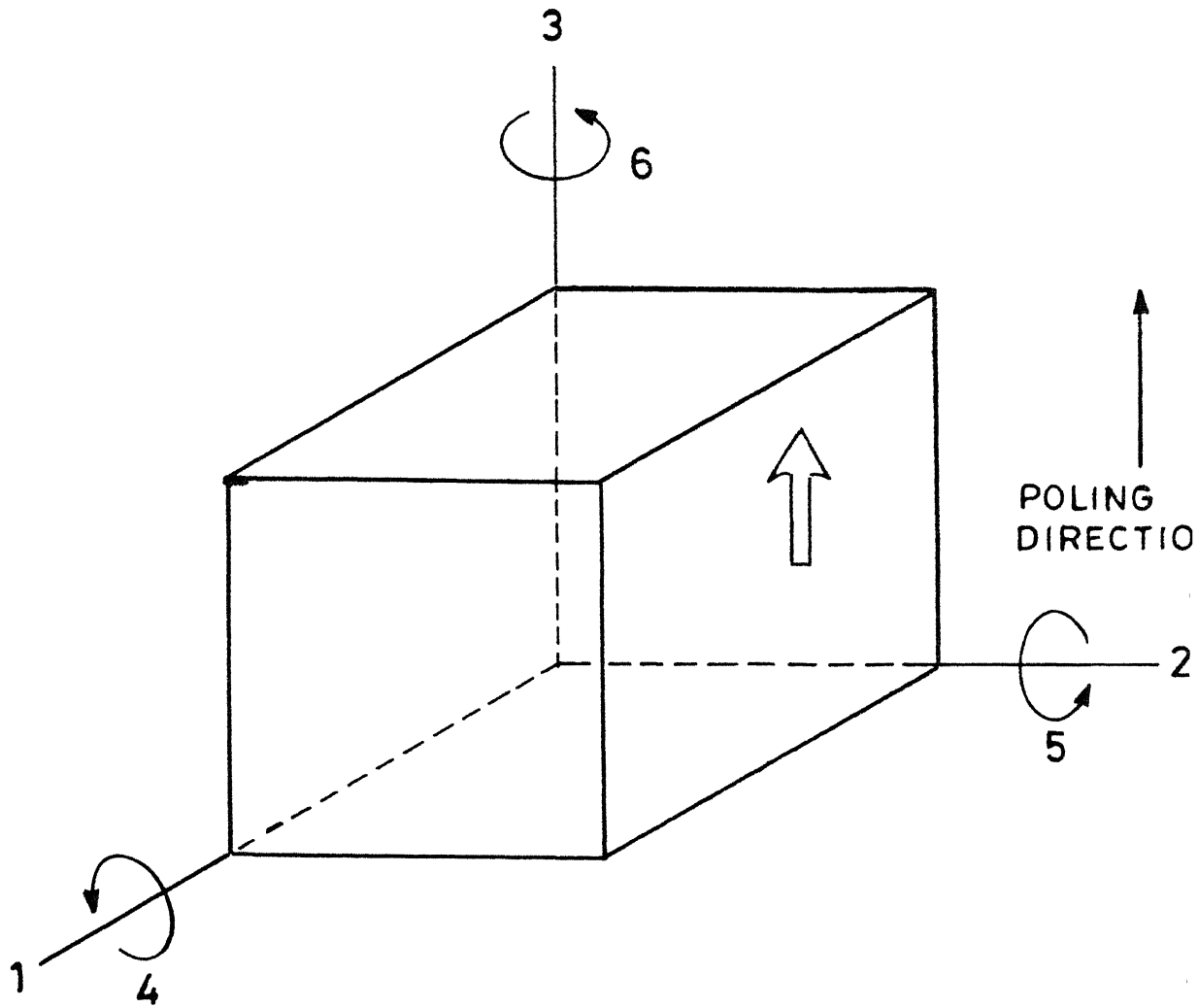
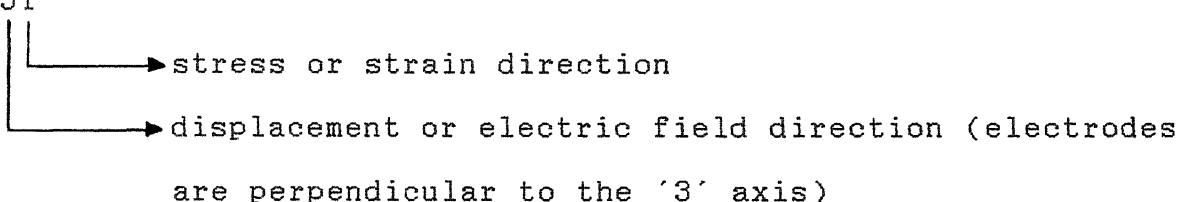


Fig. 1.1 Notation of axis for poled ceramic element.

second to the mechanical direction (stress or strain). Also when a property is being measured holding another quantity constant, a superscript symbol is used to indicate the quantity held constant. The mostly used piezoelectric coefficients with appropriate subscripts and superscripts are given below:

$d_{31}$



stress or strain direction

displacement or electric field direction (electrodes are perpendicular to the '3' axis)

$S^E$  = compliance at constant electric field (electrodes shorted)

$S^D$  = compliance at constant displacement (open circuit)

$\epsilon^T$  = dielectric constant at constant stress (free)

$\epsilon^S$  = dielectric constant at constant strain (clamped)

$K^T$  = relative dielectric constant at constant stress (free)

$K^S$  = relative dielectric constant at constant strain (clamped)

$d_{33}$  = charge or strain coefficient (longitudinal);  
(charge density/applied stress, C/N;  
strain developed/applied field, m/V)

$d_{31}$  = charge or strain coefficient (lateral), m/V or C/N

$s_{31}^2$  = Mechanical Compliance (lateral), m<sup>2</sup>/N



$g_{31}$	=	voltage coefficient (lateral),	$\frac{V-m}{N}$	8
		(open circuit field/applied stress)		
$K_3$	=	relative dielectric constant, longitudinal,		
		no units ( $K_3 = K_{33} = \frac{\epsilon_{33}}{\epsilon_0}$ )		
$k_{33}$	=	electromechanical coupling factor (longitudinal),		
		no units		
$k_{31}$	=	electromechanical coupling factor (lateral),		
		no units		
$k_p$	=	electromechanical coupling factor, planer (radial),		
		no units (thin disk only).		

### 1.3 Piezoelectricity in Ceramics

Crystalline ceramics are randomly oriented grains intimately bonded together forming the solid. Even though the individual crystals in a ceramic may be strongly piezoelectric, the random orientation of the crystals cancel the piezoelectric effect of the individual grains. If the dipoles can be oriented in a particular direction by the application of electric field, then this orientation of dipoles would impart piezoelectric property to the ceramic. However in some crystals (e.g., Tourmaline, Hexagonal CdS etc.) electric field higher than break down field is necessary for reversing the dipoles so that this process can not be used to impart piezoelectricity. Thus spontaneous

polarisation and reversibility under electric field of a magnitude less than the break down field are necessary for developing piezoelectric properties. Ferroelectric ceramics are (fig.1.2) characterised by spontaneous and reversible polarisation by low electric field. After sintering when the ceramic is cooled down from high temperature to room temperature it undergoes conversion from pyroelectric phase to ferroelectric phase accompanied by elongation of the crystal in the direction of dipoles. This gives rise to intergranular stresses. To minimise these stresses ferroelectric domains are formed within which all the dipoles are aligned in the same direction.

Application of an electric field (called poling) orients these domains in the direction of electric field and develops piezoelectric properties.

Ferroelectric ceramics due to their following characteristic properties have become very useful in device applications. These properties include 1) High dielectric constant, 2) High piezoelectric constants, 3) Relatively low dielectric loss, 4) High electrical resistivity, 5) Moisture insensitivity, 6) High electromechanical coupling coefficient, 7) Medium hardness and in some cases, 8) High optical transparency and 9) High electro-optic coefficients.

The basis for the existence of ferroelectricity rests primarily on structural (symmetry) considerations. The number

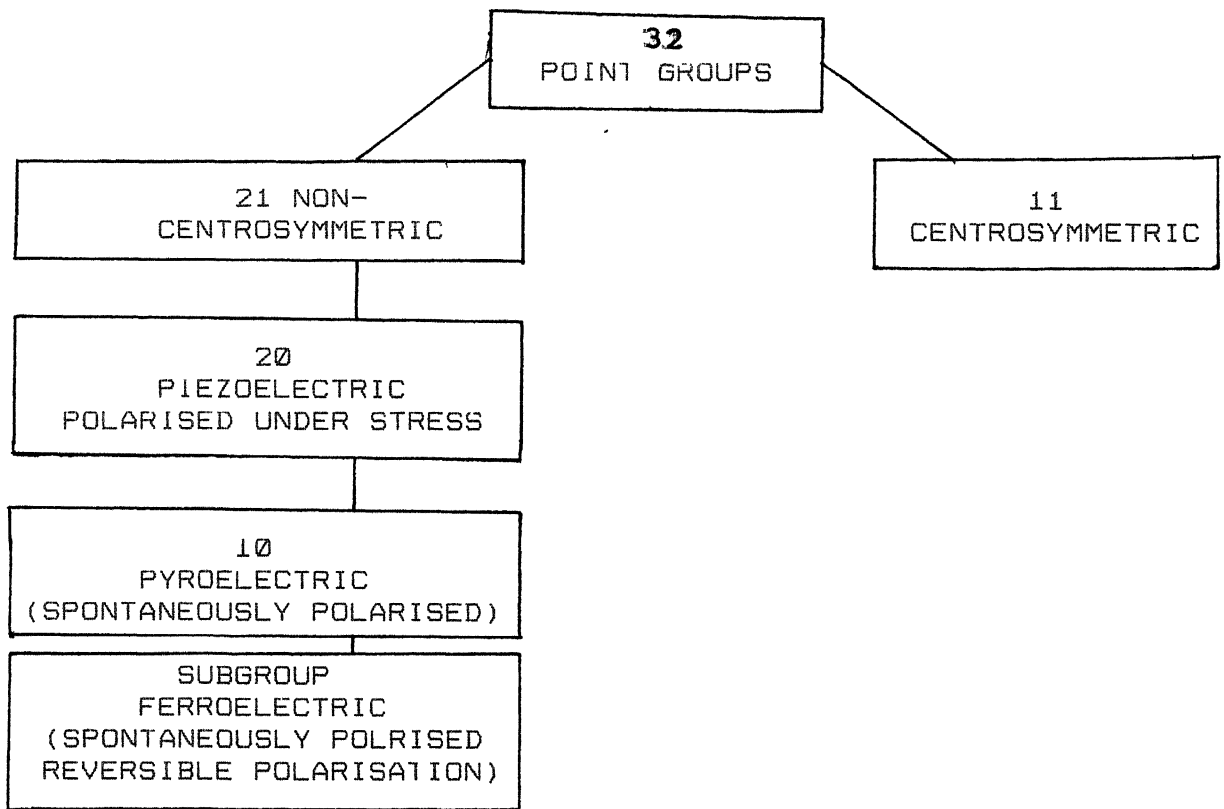


Figure 1.2 : Interrelationship of piezoelectrics crystals and subgroups on the basis of internal crystal symmetry

of actual ferroelectrics today are known to be thousands when one includes the large number of solid solution compositions. Ferroelectricity was first discovered in Rochelle salt by Valesek in 1920. Further significant developments in the history of ferroelectric materials came in the 1940s when ferroelectricity was discovered in single crystal and in polycrystalline barium titanate ( $\text{BaTiO}_3$ ), ceramics. In 1950s the

ferroelectric lead-zirconate-titanate, [PZT], ceramic solid solution compositions developed [5] into most promising piezoelectric ceramic material. Before the discovery of  $\text{BaTiO}_3$  piezoelectric ceramic,  $\text{TiO}_2$  with dielectric constant, 100, was known to be the best dielectric material.  $\text{BaTiO}_3$  with dielectric constant, 1100, is still widely used for device application because of high stability over wider temperature range as compared to any other previously known materials.

Barium titanate has a perovskite structure (fig. 1.3). The ideal perovskite structure is cubic with titanium ion at the body centre, barium ions at the cube corners and oxygen ions at the face centres of the cube. The  $[\text{TiO}_6]^{+8}$  octahedra extend indefinitely in three dimensions to form the main skeleton of the structure.

For many compounds, including  $\text{BaTiO}_3$ , the cubic structure is stable only at high temperature. On cooling distortions from the cubic structure are produced with  $\text{Ti}^{+4}$  ion displaced slightly off centre giving rise to tetragonal structure (fig.1.4). This

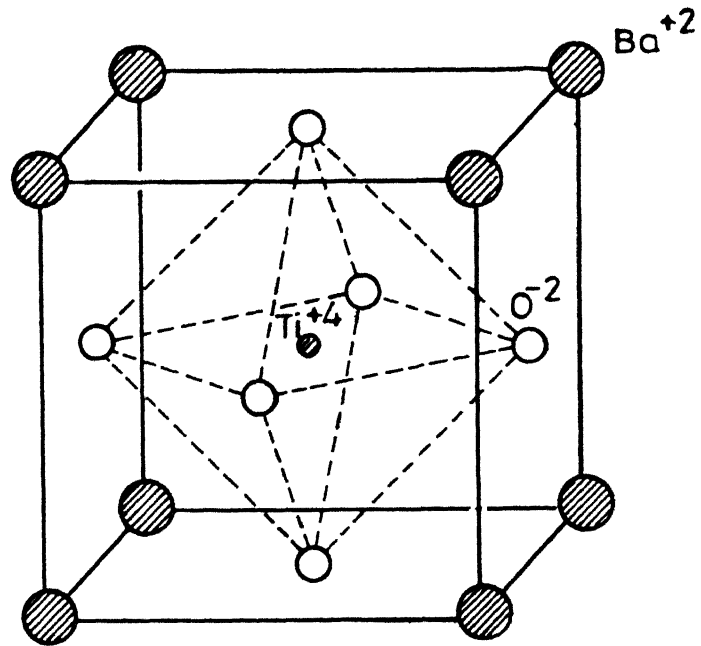


Fig.1.3 The perovskite structure as typified by  $\text{BaTiO}_3$  above Curie temperature.

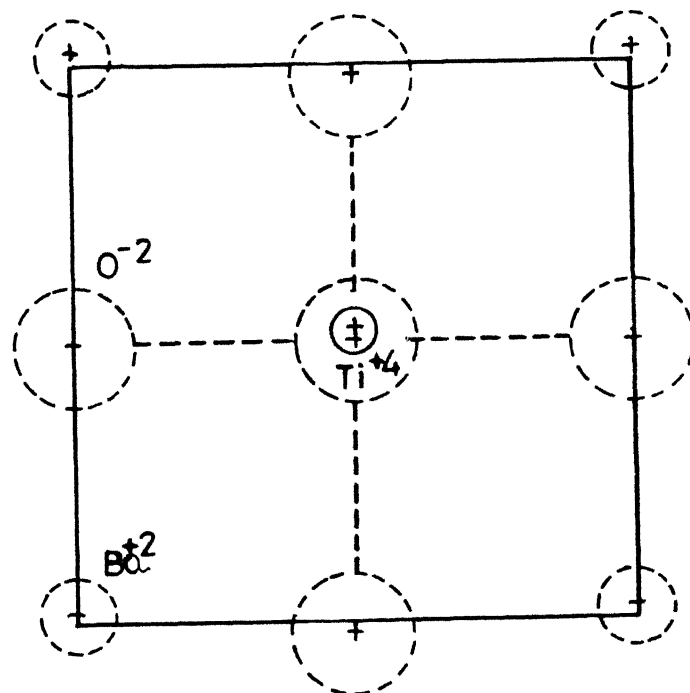


Fig.1.4 Ions position in tetragonal  $\text{BaTiO}_3$ . [7]

produces the distorted acentric  $[\text{TiO}_6]^{-8}$  octahedra and gives rise to an electric dipole moment.

In  $\text{PbTiO}_3$ , the  $\text{TiO}_6$  and  $\text{PbO}_{12}$  polyhedra are more distorted than in  $\text{BaTiO}_3$ . This is shown in figure 1.5.

Hence the polar character of  $\text{PbTiO}_3$  is more pronounced than that of  $\text{BaTiO}_3$  and their Curie temperatures are  $490^\circ\text{C}$  and  $120^\circ\text{C}$  respectively. The discovery of high dielectric constant in ferroelectric ceramics rocketed the investigations in this area.

#### 1.4 PZT Piezoelectric Ceramics:

The discovery of very strong and stable piezoelectric effect in PZT solid solution [6] in 1954 gave a jolt to the researchers in this field. Higher Curie temperature of PZT ( $360^\circ\text{C}$ ) over  $\text{BaTiO}_3$  ( $120^\circ\text{C}$ ) gave stable piezoelectric properties over a wide range of temperature. Doped PZT ceramics on the other hand give much improved properties over pure PZT ceramics [5] and finds a wide range of application in transducers, wave filters, high voltage source, sounders etc.

PZT is a solid solution of lead-zirconate (rhombohedral) and lead-titanate (tetragonal) with varying degree of composition. The generalised chemical formula is  $\text{Pb}(\text{Zr}_x\text{Ti}_{1-x})\text{O}_3$  where  $0 < x < 1$ .

Esturo Sawaguchi [8] first developed the phase diagram of the solid solution of  $\text{PbZrO}_3$ - $\text{PbTiO}_3$  system. He established

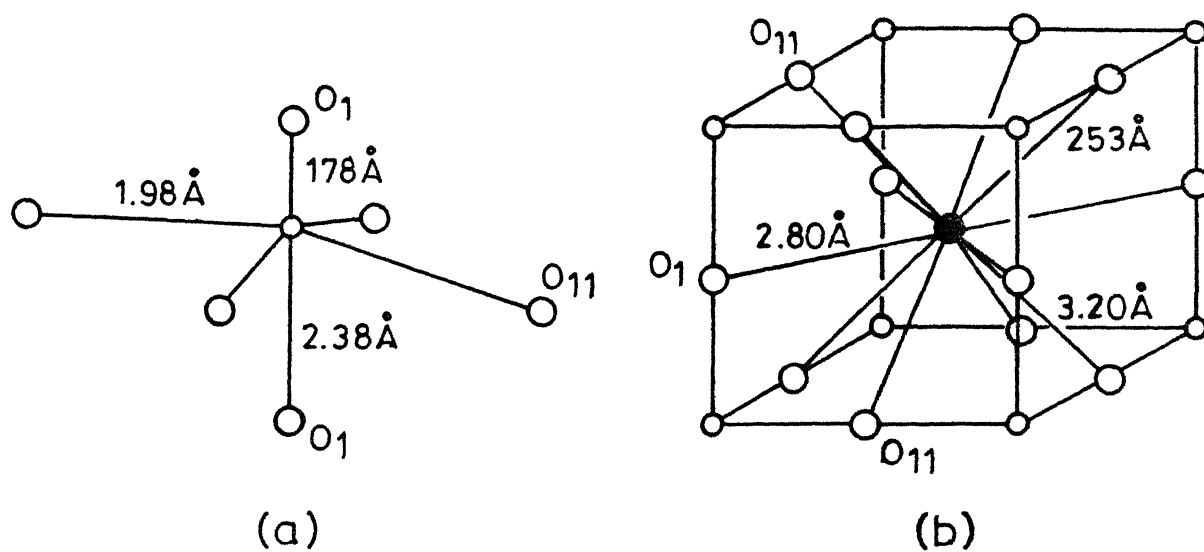


Fig.1.5 Distortions in (a) the  $\text{TiO}_6$  and (b) the  $\text{PbO}_{12}$  coordination polyhedra of tetragonal  $\text{PbTiO}_3$ . The two crystallographically distinct oxygens are labelled here  $\text{O}_1$  and  $\text{O}_{11}$ . [65]

that substitution of  $\text{Zr}^{+4}$  for  $\text{Ti}^{+4}$  in  $\text{PbTiO}_3$  reduces the tetragonal distortion (fig. 1.6) and ultimately causes the appearances of another ferroelectric phase of rhombohedral ( $R.3m$ ) symmetry. The boundary between tetragonal and rhombohedral phases is nearly independent of temperature (morphotropic). Still more  $\text{Zr}^{+4}$  causes the appearance of the orthorhombic antiferroelectric  $\text{PbZrO}_3$  phase [9]. Its exact extent is rather impurity sensitive. The current version of phase diagram (fig.1.7) is determined with zirconia containing low amount of hafnia.

The rhombohedral ferroelectric phase actually divides into two phases [10] shown by measurement of both electrical properties and thermal expansion, although both appear to be simple rhombohedral cell by X-ray diffraction. Neutron diffraction studies indicate a multiple rhombohedral cell for the low temperature phase [11].

Morphotropic phase boundary (MPB) in PZT ceramics is the tetragonal-rhombohedral phase boundary. This 'phase boundary' is considered at that composition where the two phases are present in equal quantity. Initially, it was thought that tetragonal-rhombohedral phase boundary corresponds to a specific composition. Later many researchers showed it to be a range of compositions and not a specific one.

P. Ari-Gur and L. Benguigui showed by means of X-ray diffraction the co-existence region to be a wide range of



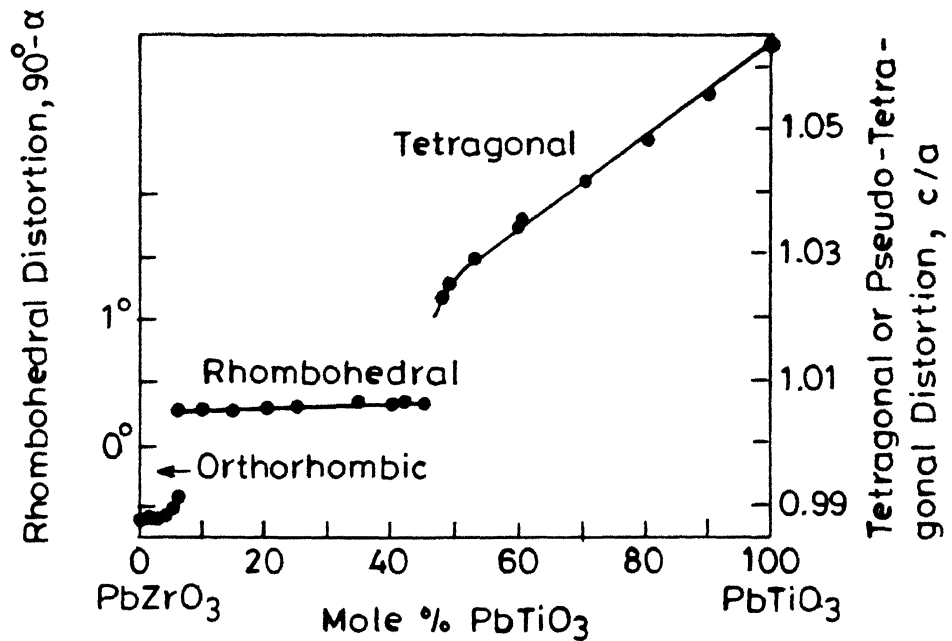


Fig. 1.6 Unit cell distortion at room temperature for the  $\text{PbTiO}_3$  -  $\text{PbZrO}_3$  system. [5]

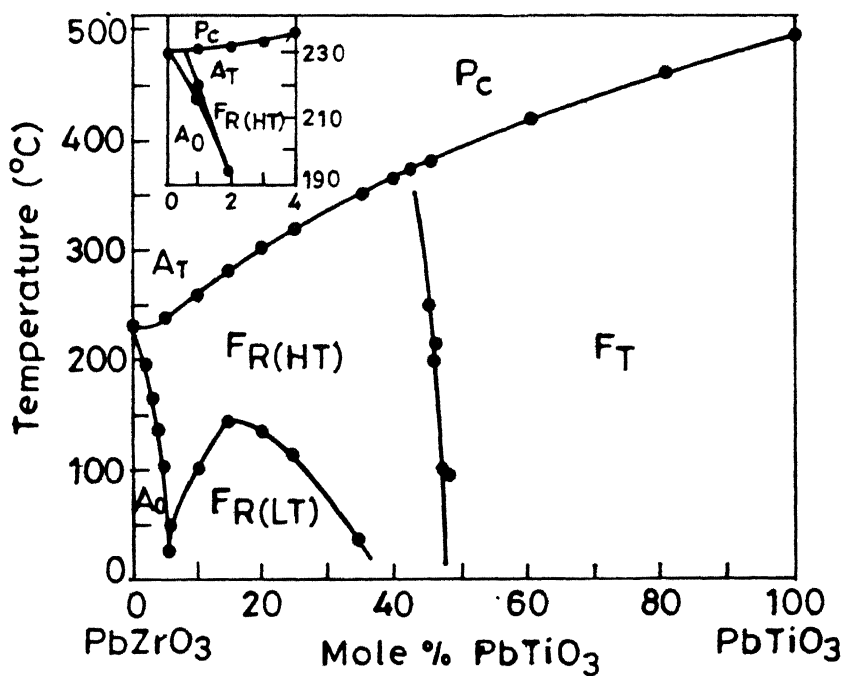


Fig. 1.7  $\text{PbTiO}_3$  -  $\text{PbZrO}_3$  sub-solidus phase diagram. [5]

compositions [12]. The lattice parameter within this range is independent of 'x' (concentration of  $ZrO_2$ ). Mabud [13] showed that MPB is a range of compositions whose width depend upon the firing temperature and time. He observed the width to be 4 mole percent ( $x \propto x = 0.04$ ) where as Gur et al [12] observed it to be as large as 15 mole percent.

The solid state reactions leading to the formation of PZT solid solution have been studied by many investigators but with differing conclusions. Matsuo and Sasaki [14] did not observed formation of PZ as an intermediate phase. According to them when  $PbO$ ,  $TiO_2$  and  $ZrO_2$  in the molar ratio 2:1:1 is heated;  $PbO$  and  $TiO_2$  react to form  $PbTiO_3$  almost completely at  $650^\circ C$ . The reaction  $PbTiO_3 + PbO + ZrO_2 \longrightarrow Pb(Zr_x Ti_{1-x})O_3$  starts near  $650^\circ C$ . In this reactions soon as  $ZrO_2$  starts to react with  $PbO$ ,  $PbTiO_3$  reacts to form  $Pb(Zr_x Ti_{1-x})O_3$  solid solution. The formation of this solid solution increases steadily with time and temperature. T. Ohno et al [15] observed synthesization of PZT only after the formation of PZ and PT as intermediate phase. The reaction sequence given by Speri and Hankey and Biggers [16] is (i)  $P + T = PT$ , (ii)  $P + PT + Z = P(SS)$ , iii)  $PT + P(SS) = PZT$ . The final stages of the reaction particularly the composition however was not discussed by these workers. Chandratreya et al [17] reported the diffusion of various ionic species to form the solid solution. X-ray and DTA analysis shows that PT begins to form at  $450^\circ C$  and finishes at

600°C and is exothermic in nature. They observed PZT to form at 715°C which was over at 785°C. But they did not observe the formation of PZ. Consequently they ruled out the PZT formation based on initial formation of PT and PZ in large amount followed by interdiffusion of  $Ti^{+4}$  and  $Zr^{+4}$  ions. They suggested that three reactants  $PbO$ ,  $ZrO_2$  and PT form reactive substances and by coupled reactive exchange of  $Zr^{+4}$  and  $2Pb^{+2}$  at  $ZrO_2/PT$  and  $Ti^{+4}$  and  $2Pb^{+2}$  at the PT/ $PbO$  interfaces followed by counter diffusion of  $Zr^{+4}$  and  $Ti^{+4}$  within the perovskite lattice.

B.V. Hiremath et al [18] suggested the following reaction sequence:

- i)  $PbO + TiO_2 = PbTiO_3$
- ii)  $PbO \text{ or } PbO(ss) + ZrO_2 = PbZrO_3 \text{ or } PbZrO_3 - \text{rich}$   
intermediate compound
- iii)  $PbTiO_3 + \text{Remaining } ZrO_2 = Pb(ZrTi)O_3 \text{ solid solution}$   
intermediate rich in PT
- iv) The intermediate products from either step (i) or step (iii) above, react with the product of step (ii). The resulting PZT solid solution has a distribution of Zr/Ti ratios determined by the previous steps.
- v) The solid solution homogenises resulting in narrow composition fluctuation.

The PZT ceramics offer good piezoelectric properties over a wide range of compositions. Jaffe et al[6] reported the

excellent performance of PZT ceramics with compositions near the tetragonal rhombohedral phase boundary. They observed high value of dielectric constant and coupling coefficient as well as relatively small variation of these with changing temperature. Boundary being nearly morphotropic, temperature dependence of electromechanical properties are free from polymorphic irregularities in contrast with  $\text{BaTiO}_3$ . They observed that composition rich in  $\text{PbTiO}_3$ , causes a marked decrease in the response because increasing c/a ratio hinders alignment of the domains.

Therefore a composition which lies in the MPB region is of particular commercial interest. Hence subsequent work has centred mainly around the MPB compositions.

### 1.5 Processing Parameters of PZT Ceramics:

Now-a-days PZT ceramics are fabricated by the following processes:

- i) Conventional solid-state sintering or mixed oxide process
- ii) Spray decomposition
- iii) Coprecipitation
- iv) Coating
- v) Sol-gel.

Commercial way of fabrication of PZT is 'conventional solid state sintering process'. The author has followed this process for fabricating the test materials. Hence discussion will be

restricted to this process only.

Conventional solid state sintering process for other ceramic system, specially for nonvolatile system creates no problem and appears to be very simple. But in PZT system, PbO creates problem. Melting point of PbO is 888 C and its vapour pressure is appreciable [18] at high temperature. This counts for appreciable amount of lead loss at the calcination and sintering temperature and leads to nonstoichiometry in the PZT compositions. Deficiency of PbO in the PZT body seriously hamper the piezoelectric properties [19]. Approximate flow sheet for fabrication of PZT by this process is given in fig. 1.8. The parameters which are of most important are listed below:

- 1) Raw materials' purity and particle size,
- i) Way of mixing,
- iii) Type of liquid used to make a slurry,
- iv) Time of mixing,
- v) Time and temperature of drying of the mixed oxide powder,
- vi) Pressure used during the compaction of the pellets,
- vii) Calcining temperature and time,
- viii) Rate of heating,
- ix) Sintering atmosphere & composition of atmosphere powder,
- x) Sintering temperature and time,
- xi) Soaking period,
- xii) Use of dopants as processing aids.

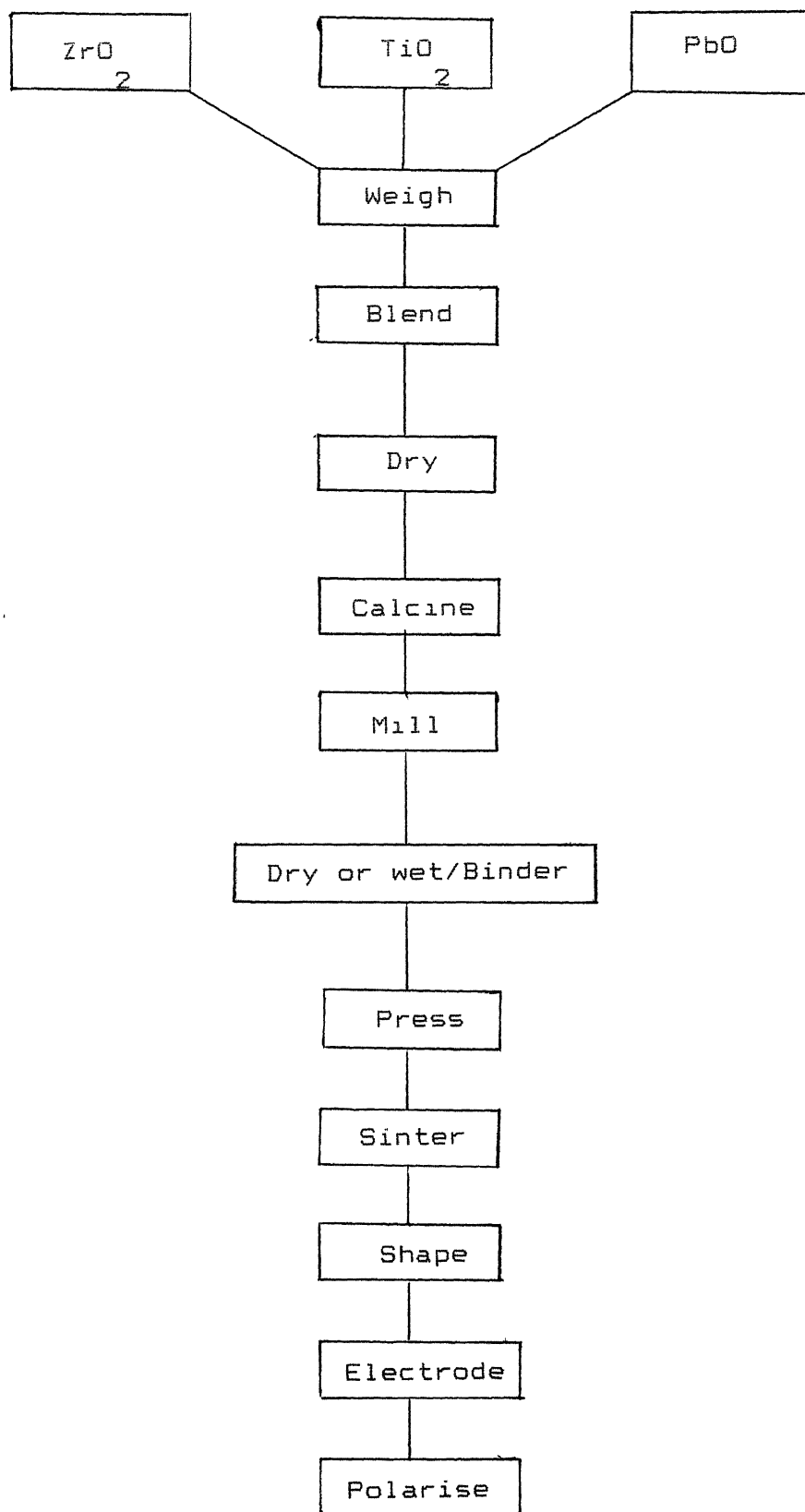


Fig. 1.8 : Flow sheet for solid state processing of PZT ceramics

Slight change in the four parameters, viz. (ii), (iii), (iv) and (v) do not affect the end property of the PZT ceramics significantly. But the rest have enormous effect.

Raw materials for  $\text{PbO}$ ,  $\text{ZrO}_2$  and  $\text{TiO}_2$  must be as pure as possible. Particle size should be within a certain range. Dana L. Hankey and James V. Biggers [20] showed the rate constant for solid state reactions for  $\text{PbZrO}_3$  formation was increased by a factor of 1.5 by decreasing the particle size of  $\text{ZrO}_2$  from 2.0 micron (plasma processed) to 0.6 micron (attrition milled). They also showed that rate constant for solid state reaction for the formation of  $\text{PbTiO}_3$  was increased by a factor of three when the packing pressure was increased from 0 to 206 MPa. The rate constant for compressing with 0, 103, 173 and 206 MPa pressure were 1.5, 3.1, 3.2 and  $4.4 \times 10^{-5}$  per second respectively.

Mixing of the particles of  $\text{PbO}$ ,  $\text{TiO}_2$  and  $\text{ZrO}_2$  is of great concern for the homogeneity of the end product. Various authors [21-23] have shown methods to determine the compositional fluctuations using powder X-ray diffraction technique. By this method it was revealed that the width of compositional fluctuation extends from 10% to 30% for  $\text{Pb}(\text{Zr}_x \text{Ti}_{1-x})\text{O}_3$  prepared by ordinary dry method. This compositional fluctuation can be reduced by careful control of all the steps. Authors [22-24] have suggested various means to produce PZT with reduced or even no-compositional fluctuation.

It was mentioned earlier that the volatilisation of PbO becomes appreciable at higher temperature. This has become a stumbling block to the reproducible production of high quality PZT ceramics. It is known that loss of PbO and resultant variation in composition affect both densification process and intrinsic electromechanical properties of the ceramic. It has been stated [25,26] that the presence of a PbO excess is critical for the achievement of high densities. Atkin and Fulrath [27] and Holman and Fulrath [28,29] discussed the use of atmosphere powders of particular compositions in the sintering enclosures, and the vapour phase equilibrium of PbO between sintering compact and atmosphere powder. According to them that it is particularly convenient to sinter a PZT compact in the presence of an atmosphere powder which has a fixed PbO vapour pressure over a range of PbO contents. The PbO content refers to the  $\text{PbO}/(\text{Zr}, \text{Ti})$  ratio. Atkin and Fulrath [27] using the concept of PbO activity (ratio of partial pressure of PbO over the PZT compact to the vapour pressure of PbO over PbO only), and the composition - temperature and composition - activity phase diagram of  $\text{PbO}-\text{TiO}_2$  and  $\text{PbO}-\text{ZrO}_2$  (fig. 1.9) showed that the closed atmosphere retains a fixed PbO activity. Thus the PZT compact independent of its initial PbO content can equilibrate to a fixed PbO content.

A.I. Kingon and J.B. Clark [30] studied in detail the atmosphere control during the sintering of PZT. According to them the PbO activity of the PZT compact is a function of the



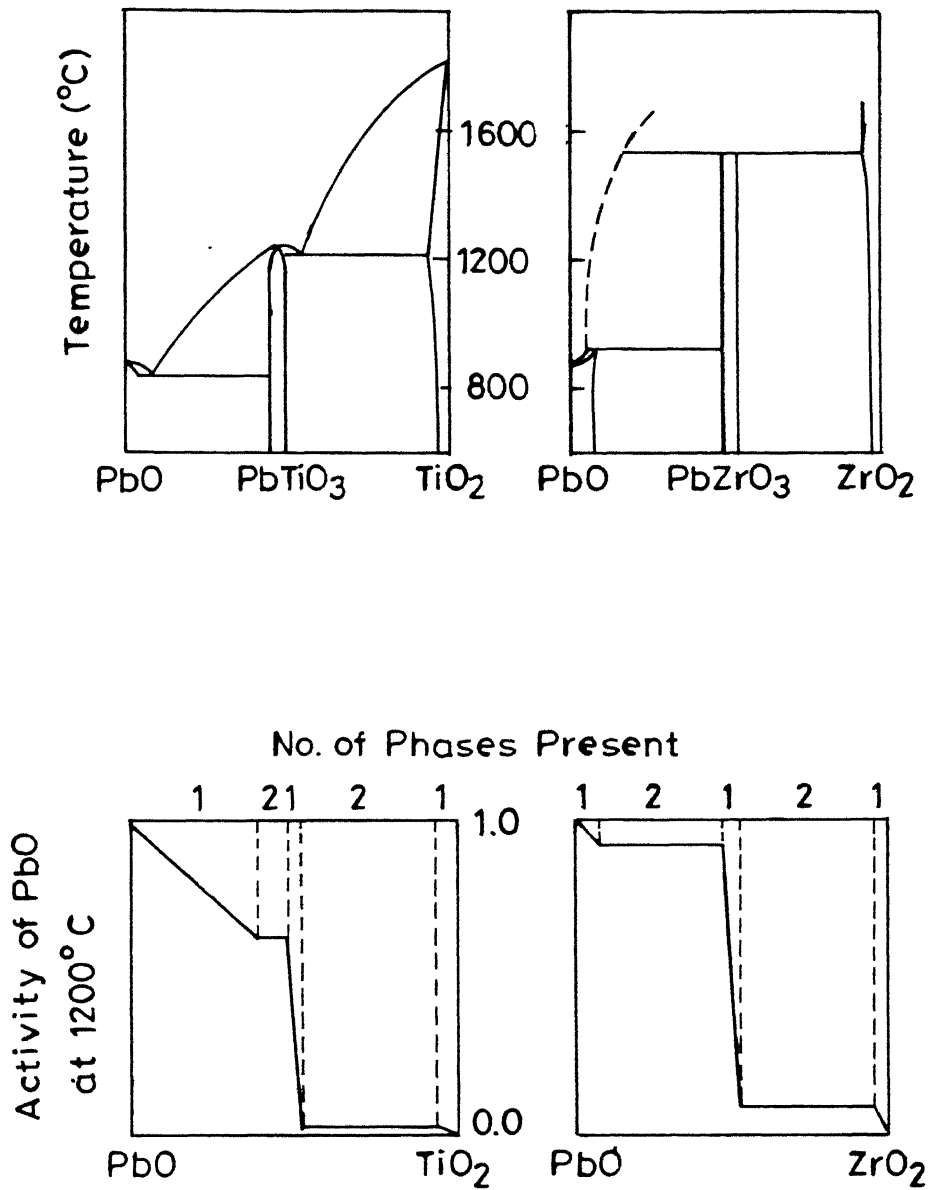


Fig. 1.9 Composition-temperature and composition-activity of PbO-TiO<sub>2</sub> and PbO-ZrO<sub>2</sub> system. [27]

excess PbO content contradicting the previous reports. They showed that with PZ + Z  $[(\text{PbZrO}_3 + 10\% \text{ZrO}_2)]$  and PZT + ZT  $[\text{Pb}_{0.525}(\text{Zr}_{0.475}\text{Ti})\text{O}_3 + (\text{Zr, Ti})\text{O}_3]$  atmosphere powder the PZT compact under closed atmosphere equilibrates to yield 0.8% and 1.6% PbO deficient PZT compacts respectively. The PZT compact with 0.1%, 3% and 19% excess in PbO equilibrated with atmosphere powder PZ + P  $(\text{PbZrO}_3 + 10 \text{ wt\% PbO excess})$  and resulted in increase in weight for 0.1% and 3% excess PbO but decrease in weight for 19% excess PbO under isothermal run due to vapour phase transfer of PbO from atmosphere powder to PZT compact. This is direct confirmation that PbO activity of  $\text{Pb}(\text{Zr,Ti})\text{O}_3$  + PbO increases with increasing excess PbO. However, PbO content are less reproducible for PZT compositions which contain a PbO excess. This excess PbO causes the liquid phase sintering which substantially enhances the initial and intermediate stage of sintering [31]. But in the final stage of sintering the presence of this liquid phase lowers the densification rate. On the other hand an increasing defect concentration due to an increasing PbO deficiency increases the densification rate during final stage of sintering.

Calcination and sintering are the most important parameter for the preparation of good ferroelectric PZT ceramics. D.A. Buckner and P.D. Wilcox [32] concluded from their work that it was important to establish the correct calcining condition. According to them the practice of controlling final density by

proper selection of the calcining condition is a more positive method than the method of adjusting the sintering condition. The optimum calcining temperature can be expected to lie within a broad temperature range near  $900^{\circ}\text{C}$  perhaps ranging as high as  $1000^{\circ}\text{C}$ . The time required for calcining is of secondary importance (fig.1.10). In the final firing, the grain size of the ceramic is dependent on the temperature. Time is again a secondary importance (fig. 1.11).

Rate of heating is another important factor for optimum piezoelectric property. C.E. Hall and J.B. Blum [33] obtained maximum piezoelectric property by keeping heating rate  $4^{\circ}\text{C}/\text{min}$ . Charles E. Baumgartner [34] studied fast firing and conventional sintering on PZT-5 and obtained that fast firing gave a density of 7.66 gms/c.c. as compared to 7.4 gms/c.c. via conventional sintering process. He also obtained 7% higher  $d$  value.

33

## 1.6 Doping Effect in PZT Ceramics

Almost unrestricted opportunities in varying the properties of piezoceramics are given by doping additives. The different types of additives used so far in the PZT ceramics can be grouped in the table - 1 [35] as given below:

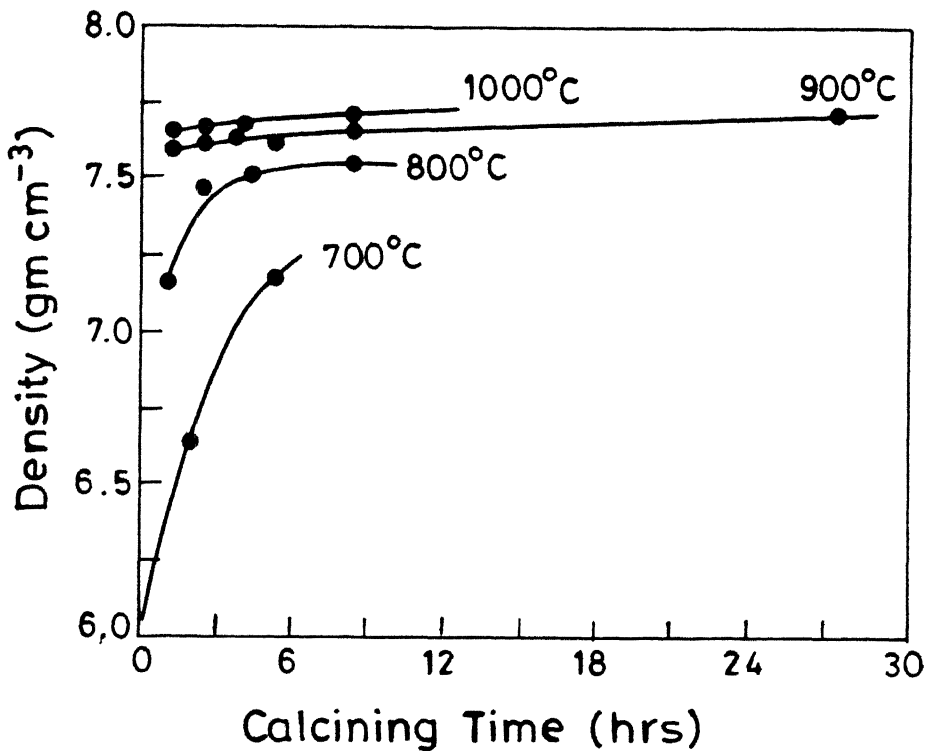


Fig. 1.10 Effect of calcination temp. on the density of end products. [32]

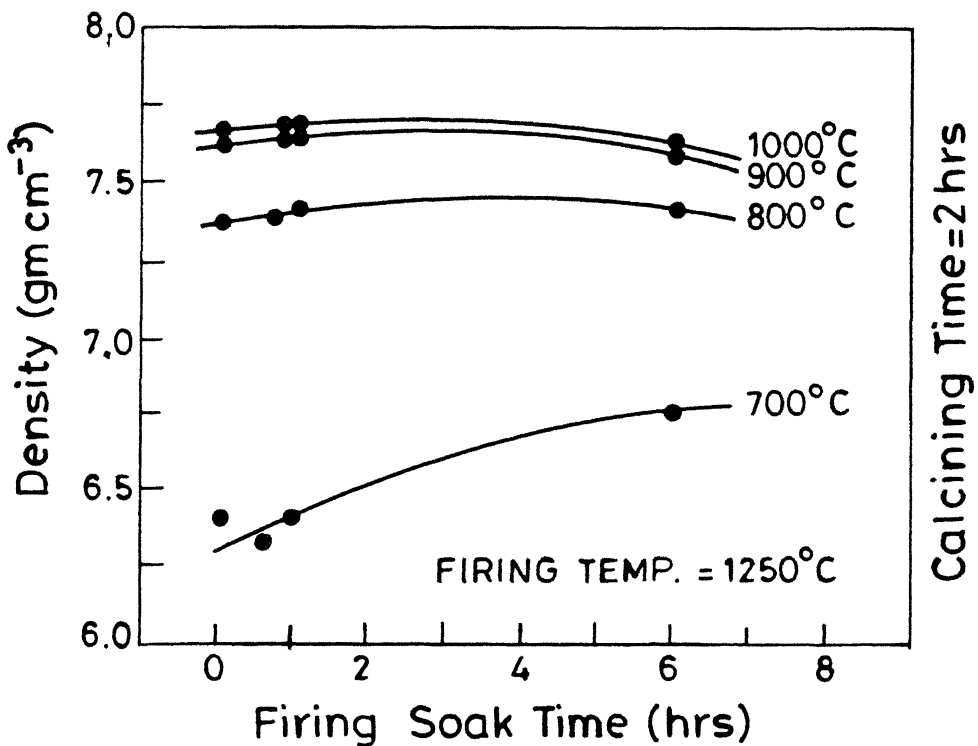
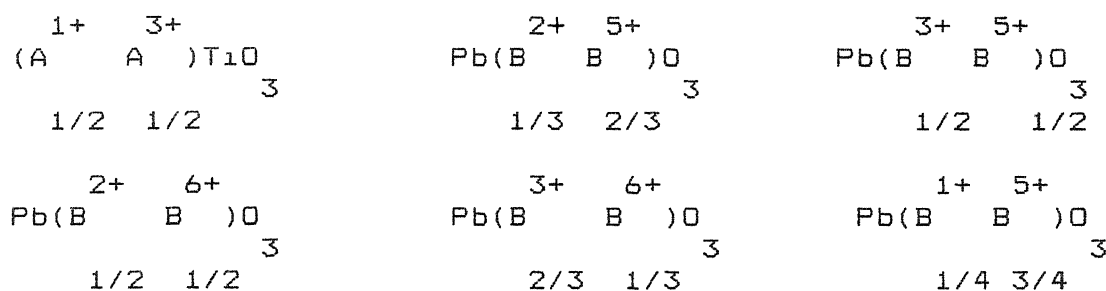
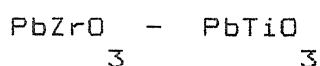


Fig. 1.11 Effect of sintering soak time on the density of end products. [32]

Table - 1.1

Some possible arrangements for the substitution of A and B sites in the perovskite structure. The dopants which go to a particular site are also given



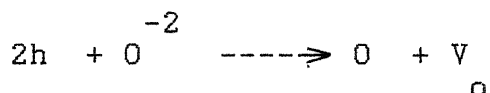
1+										
A	Li	Na	K							
3+										
A	Bi	La	Nd							
1+										
B	Li	Cu								
2+										
B	Mg	Ni	Zn	Mn	Co	Sn	Fe	Cd		
3+										
B	Mn	Sb	Al	Yb	In	Fe	Co	Se	Y	
5+										
B	Nb	Sb	Ta	Bi						
6+										
B	W	Te	Re							

---

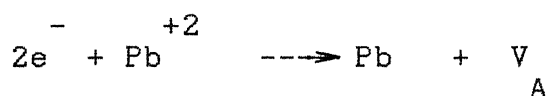
The impurities mentioned in the table-1 can be categorised into three groups [5]:

- i) Impurity acceptors :  $K^{+1}$ ,  $Na^{+1}$ ,  $Mg^{+2}$ ,  $Sc^{+3}$ ,  $Fe^{+3}$ ,  $Al^{3+}$  etc.
- ii) Impurity donors :  $La^{+3}$ ,  $Bi^{+3}$ ,  $Nb^{+5}$ ,  $Ta^{+5}$ ,  $Sb^{+5}$ ,  
 $W^{+6}$ , etc.
- iii) Other isovalent substituting impurity ions :  $Sr^{2+}$ ,  $Ca^{2+}$ , etc.

Ion valency of the acceptor ions are lower than those of substituted ions in  $ABO_3$  perovskite crystals. It contributes fewer electrons to the structure than the ions it replaces, thus creating holes whose consequence is the creation of oxygen vacancies



on the other hand, ion valency of the donor ions are higher than those of substituted ions. These contributes extra electrons to the structure which leads to creation of A-site, i.e. lead vacancies



isovalent substitution does not create any vacancy.

Though the donor ions create vacancies in A-site but depending on the increase of partial pressure of  $PbO$  B-site vacancies can also be created [36]. In an investigation of the addition of  $La_2O_3$  to  $PbTiO_3$  in relation to the partial pressure

of  $PbO$ , Detlev Hennings [37] showed that specimens with only A-site vacancies could be produced at low partial pressure of  $PbO$ .

As the partial pressure of  $PbO$  is increased, the concentration of A-site vacancies decrease and that of B-site vacancies increase, as expected. However partial pressure of  $PbO$  can not be increased arbitrarily. It is naturally limited by the condensation of  $PbO$  as a liquid phase at the grain boundaries of the ceramic.

P. Gonnard and M. Troccaz [38] showed that donor impurity ions not necessarily always occupy completely the A-sites only. Their theoretical model supported by experimental proof showed that the distribution of an ion on the A and B sites was a regular function of ionic radius. This type of dopant distribution has direct impact on the piezoelectric properties of the PZT ceramics.

It is mentioned earlier that piezoelectric properties of PZT ceramics are enormously changed by the introduction of dopants. T. Roy Chowdhury and S.B. Deshpande [39] doped three valent ions ( $La^{+3}$ ,  $Pr^{+3}$ ,  $Nd^{+3}$ ) and five valent ions ( $Nb^{+5}$ ,  $Ta^{+5}$ ) and observed that with increasing concentration of +3 valent ions  $T_c$  (Curie temperature) reduces very much, dielectric constant improves,  $d_{31}$  increases at a lower concentration but decreases at higher concentration.  $k_p$  improves at lower concentration but again reduces with increasing concentration of dopants. For five valent dopants dielectric constant and  $d_{31}$  increases but Curie temperature reduces,  $k_p$  after initial increase gradually reduces. Frank Frank Kulcsar [40] studied the effect of  $La_2O_3$ ,  $Nd_2O_3$

$\text{Nb}_2\text{O}_5$ ,  $\text{Ta}_2\text{O}_5$  on PZT compositions near morphotropic phase boundary. Modified ceramics showed  $k_p$  of about 0.50 and substantially increased dielectric constant upto 1545.  $Q_M$  decreased to about 70. Volume resistivity increased at temperature upto 500°C,  $T_c$  also decreased.

S. Takahashi and M. Takahashi [41] studied the effect of impurities on the Mechanical Quality factor (reciprocal of internal friction) of PZT. The observed impurities like  $\text{La}_2\text{O}_3$ ,

$\text{Nb}_2\text{O}_5$ ,  $\text{Ta}_2\text{O}_5$ ,  $\text{Sb}_2\text{O}_3$ ,  $\text{Bi}_2\text{O}_3$ ,  $\text{WO}_3$  and  $\text{ThO}_2$  decrease the values of

$Q_M$ . It seems that the impurities give rise to the formation of

vacancies in the Pb positions making domain wall remarkably mobile and increasing internal friction. On the other hand  $\text{Na}_2\text{O}$ ,

$\text{K}_2\text{O}$ ,  $\text{Ga}_2\text{O}_3$ ,  $\text{In}_2\text{O}_3$ ,  $\text{Cr}_2\text{O}_3$ ,  $\text{Fe}_2\text{O}_3$ ,  $\text{Co}_2\text{O}_3$ ,  $\text{NiO}$ ,  $\text{Rh}_2\text{O}_3$ ,  $\text{IrO}_2$  and  $\text{U}_3\text{O}_8$

increases the value of  $Q_M$ .

The group characteristics of entire donor impurities and acceptor impurities given by Jaffe [5] are

Donor impurities	Acceptor impurities
1. Relatively low dielectric constant	1. Increased dielectric constant
2. Low dielectric loss	2. High dielectric loss
3. Moderately lower electrical volume resistivity	3. Higher electrical volume resistivity
4. High $Q_M$	4. Low $Q_M$
5. High coercive field	5. Low coercive field



Effect of isovalent substitution in PZT ceramics are not thoroughly investigated. F. Kulcsar [42] studied the effect of substitution of  $Pb^{+2}$  by  $Sr^{+2}$  and  $Ca^{+2}$ . According to him every atom percent addition of either of these divalent impurities lowers the Curie temperature about  $9.5^{\circ}C$  but raises the dielectric constant at room temperature. Coupling factor and elastic modulus are not greatly affected. It slightly raises  $d_{33}$ . F. Kulcsar [43] again studied the effect of substitution of

B-site ions by  $Th^{+4}$  (ionic radius  $0.99 \text{ \AA}$ ) in PZT. The effect of this ion is comparable with that of  $Nb^{+5}$  or  $La^{+3}$  ions. The results are given in the table - 1.2

**Table 1.2**  
**Compositions and Properties**

Composition					Fired density	Dielectric constant	Dissipation factor (D%)	k p
					gms/c.c	at 1 kc/s	at 1kc/s	
Pb	Th	(Zr	Ti	)O	7.83	1560	1.5	0.56
.988	.006	.52	.48	3				
Pb(Zr	Ti	)O <sub>3</sub>	+1wt%Nb	O <sub>2.5</sub>	7.43	1371	1.4	0.53
.53	.47							
Pb(Zr	Ti	)O <sub>3</sub>	+1wt%La	O <sub>2.3</sub>	7.46	1483	2.0	0.53
.54	.46							

Thus though substitution in A-site does not much improve the quality of PZT ceramics, the isovalent substitution in B-site has improved the properties.

The author did not find any work on the effect of isovalent substitution of cerium oxide ( $\text{CeO}_2$ ) in PZT ceramics.  $\text{CeO}_2$  has the characteristic capability of dissolving in zirconia to form stabilized zirconia (cubic solid solution). More than 20 mole percent ceria in zirconia forces monoclinic zirconia to be converted into cubic structure which is stabilized zirconia. Thus the study of the effect of substitution of zirconia by ceria in PZT ceramics can be an interesting work. Ionic radius of  $\text{Ce}^{+4}$  ( $0.92 \text{ \AA}$ ) is closer to that of  $\text{Zr}^{+4}$  ( $0.84 \text{ \AA}$ ). According to the model of P. Gonnard and M. Troccaz [38] though most of the substituted  $\text{Ce}^{+4}$  should occupy the B-site some amount should also occupy the A-site which means the elimination of  $\text{Pb}^{+2}$  to a very small extent from the A-site of perovskite structure. According to their theoretical model the distribution of occupancy is about 17% A-site and 83% B-site. Hence the author has selected  $\text{CeO}_2$  as the doping impurity in PZT ceramics. Composition was selected at  $x = 0.535$  and ceria was doped at different concentrations replacing zirconia. Some interesting results regarding piezoelectric and mechanical properties were obtained.

## CHAPTER 2

### SAMPLE PREPARATION AND CHARACTERIZATION

#### 2.1 Sample Preparation

##### 2.1.1 Raw Materials

The raw materials used for the preparation of PZT samples are as follows:

Table 2.1

Details of Chemicals Used

Chemicals	Purity	Manufacturer
1. Lead II Oxide (Yellow) (PbO)	>99.0%	Fluka-Garantie, Switzerland
2. Zirconia ( $ZrO_2$ ) (Unstabilized)	99.5%	Indian Rare Earth Ltd. (IRE) Kerala
3. Titania ( $TiO_2$ ), [Anatase]	>99%	Fluka-Garantie, Switzerland
4. Cerium Oxide ( $CeO_2$ )	99.99%	Indian Rare Earth Ltd. (IRE), Kerala

##### 2.1.2 Preparation of Atmosphere Powder

The composition of the atmosphere powder was selected as PZ + 5 wt% PbO. The 5 wt% excess PbO was used in the atmosphere powder to maintain the stoichiometry of the PZT composition.

250 grams of batch material for the atmosphere powder was prepared by weighing PbO and  $ZrO_2$  accurately. The batch material

was put in a plastic jar. It was wet ball milled with  $Al_2O_3$

balls for 5 hours. Isopropanol was used as liquid media. It was dried in a beaker with constant stirring at  $80^{\circ}\text{C} \pm 5^{\circ}\text{C}$ . The dried power was poured in a recrystallised alumina crucible and covered with a similar crucible. The whole assembly was transferred in a pit furnace with silicon carbide heating element. It was calcined at  $860^{\circ}\text{C}$  for 4 hours. After taking out from the furnace the atmosphere powder which formed a compact was crushed to powder by agate mortar and pestle.

However X-ray examination of the powder shows that it contains PZ and free zirconia in small amount. Thus some loss of lead occurs during preparation, leading to a lead deficient powder.

### 2.1.3 Preparation of PZT Compositions

The morphotropic phase boundary in  $\text{Pb}(\text{Zr}_x \text{Ti}_{1-x})\text{O}_3$  lies at  $x \approx 0.535$ . Samples were prepared having this value of  $x$  but part of  $\text{ZrO}_2$  was replaced by  $\text{CeO}_2$  so that the composition can be represented by  $\text{Pb}(\text{Zr}_{x-\delta} \text{Ce}_{\delta} \text{Ti}_{1-x})\text{O}_3$ , with  $\delta = 0, 0.001, 0.01, 0.02$  and  $0.05$ . The molar ratios are given in table 2.2.

Table 2.2

Chemical Compositions of PZT Doped with Ceria

PbO molar ratio	ZrO <sub>2</sub> molar ratio	TiO <sub>2</sub> molar ratio	CeO <sub>2</sub> molar ratio
1.00	0.535	0.465	0.000
1.00	0.534	0.465	0.001
1.00	0.525	0.465	0.010
1.00	0.515	0.465	0.020
1.00	0.485	0.465	0.050

Two hundred grams of batch materials for each composition was prepared. Individual oxide component was weighed accurately. The steps for preparation and drying of the slurry were similar to the preparation of atmosphere powder. The dried powder was passed through 60 mesh (ASTM) screen. It was then loosely poured in the recrystallised alumina crucible. Atmosphere powder was taken in a platinum crucible. It was placed over the loose powder. The system was covered with similar alumina crucible. The total assembly is shown in figure 2.1.a. It was then put in the pit furnace. The calcination was done at 960<sup>o</sup> C for 4 hours. The approximate calcining schedule is given in table 2.3.

**Table 2.3**  
**Calcining Schedule**

Time, in hours <sup>o</sup> C	Temperature of the crucible
0	40
1	140
2	330
3	520
4	700
5	850
6	960
10	960

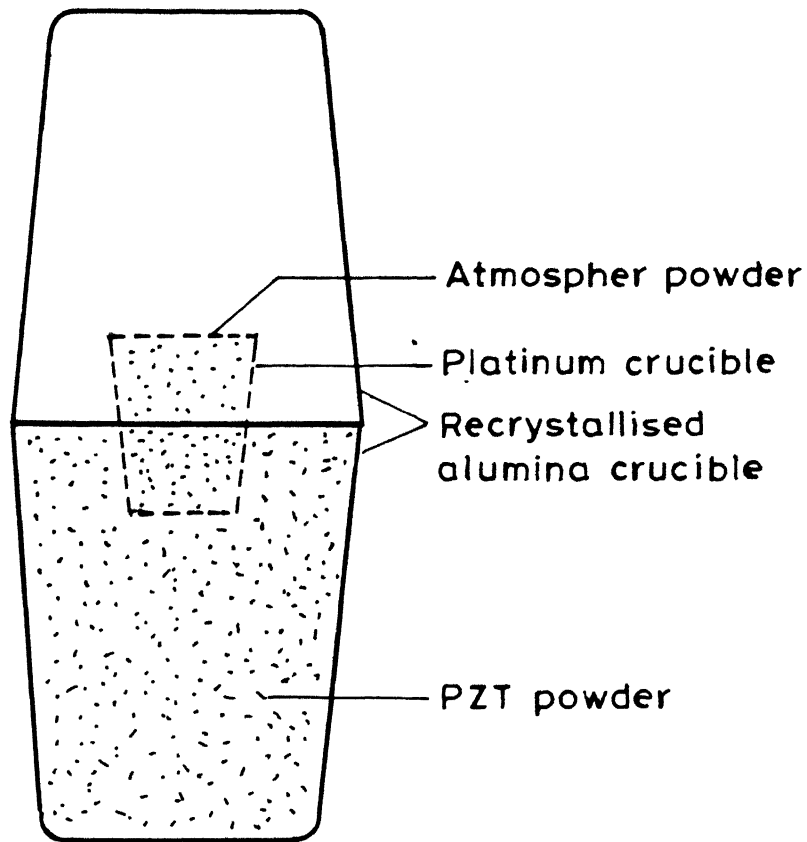


Fig.2.1(a) Schematic diagram of crucible arrangement during calcination.

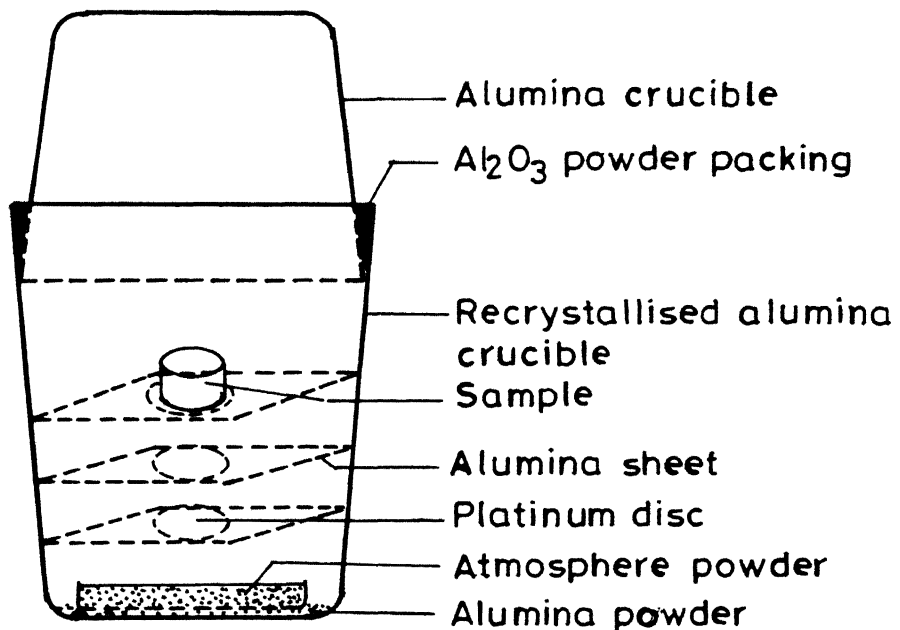


Fig.2.1(b) Schematic diagram of crucible arrangement during sintering.

The calcined aggregate of each set was crushed into powder in agate mortar and pestle. The powders were then mixed with 45 c.c. of 2.5% polyvinyl alcohol solution (PVA) and 200 c.c. of water was added to make a slurry. This slurry was ball milled for 30 minutes for good mixing of PVA. It was dried at  $60^{\circ}\text{C} \pm 5^{\circ}\text{C}$  in a glass beaker with constant stirring. The dried powder formed a lump which was crushed again in mortar pestle and passed through 60 mesh screen (ASTM). Pellets were made with fixed amount of powder (15 gms or 12 gms for 1/2" or 1" die respectively) and well compacted using 9 ton pressure in hydraulic press. The pellets were sintered at  $1200^{\circ}\text{C}$  for 4 hours. Approximate sintering schedule is given in table 2.4.

**Table 2.4**  
**Sintering Schedule**

Sintering time	Sintering temp. $^{\circ}\text{C}$ ( $^{\circ}\text{C}$ )	Soaking period
0	40	
30 min.	120	1 hr.30 mi.
2 hr. 00 min.	120	
3 hr. 00 min.	360	
3 hr. 40 min.	550	
8 hr. 40 min.	550	5 hrs.
9 hr. 40 min.	860	
10 hr. 40 min.	1030	
11 hr. 40 min.	1200	
15 hr. 40 min.	1200	4 hrs.



The configuration of the crucible arrangement during sintering is given in fig.(2.1.b). These test pellets were used for all further studies.

## 2.2 Phase Analysis

Phase analysis of the samples was carried out by X-ray diffraction technique. The specimen for X-ray was made by grinding the sintered sample in an agate mortar to fine powders. The powdered sample was packed into a rectangular perspex sample holder. The surface was smoothened by sliding and compressing with a glass slide back and forth over it. A REICH SEIFERT ISO-DEBYEFLEY 2002 DIFFRACTOMETER  $\text{CuK}\alpha$  ( $\lambda = 1.5406 \text{ \AA}$ ) radiation was used.

The X-ray diffraction patterns of the sample were taken in the  $2\theta$  range of  $20^\circ$  to  $75^\circ$  with the following operating conditions given in table 2.5.

Table 2.5

### Conditions for Operation of X-ray Diffractometer

Current, voltage	= 20 mA, 30 KV
Time constant	= 10 sec.
Beams slit width	= 1.5 mm.
Detector slit width	= 0.3 mm.
Scanning speed	= $0.6^\circ$ /min.
Chart speed	= 15 mm/min.
Full scale intensity	= 10 K counts/min

The configuration of the crucible arrangement during sintering is given in fig.(2.1.b). These test pellets were used for all further studies.

## 2.2 Phase Analysis

Phase analysis of the samples was carried out by X-ray diffraction technique. The specimen for X-ray was made by grinding the sintered sample in an agate mortar to fine powders. The powdered sample was packed into a rectangular perspex sample holder. The surface was smoothened by sliding and compressing with a glass slide back and forth over it. A REICH SEIFERT ISO-DEBYEFLEY 2002 DIFFRACTOMETER  $\text{CuK}\alpha$  ( $\lambda = 1.5406 \text{ \AA}$ ) radiation was used.

The X-ray diffraction patterns of the sample were taken in the  $2\theta$  range of  $20^\circ$  to  $75^\circ$  with the following operating conditions given in table 2.5.

Table 2.5

### Conditions for Operation of X-ray Diffractometer

Current, voltage	= 20 mA, 30 KV
Time constant	= 10 sec.
Beams slit width	= 1.5 mm.
Detector slit width	= 0.3 mm.
Scanning speed	= $0.6^\circ$ /min.
Chart speed	= 15 mm/min.
Full scale intensity	= 10 K counts/min

From the diffraction pattern (  $2\theta$  Vs. Intensity) the phases present were identified from the peak positions. The peak positions were compared with standard X-ray data files (14-31). From the peak position, lattice parameters were calculated [44] as follows:

### Tetragonal System

Interplaner spacing of tetragonal system,  $d_T$ , is given by,

$$\frac{1}{d_T^2} = \frac{h^2 + k^2}{a_T^2} + \frac{l^2}{c_T^2}$$

$h, k, l$  are Millers Indices of a particular plane  $a_T, c_T$  are the lattice constants. Combining the Braggs law with the above equation we get:

$$\sin^2 \theta = \frac{1}{4} \left( \frac{h^2 + k^2}{a_T^2} + \frac{l^2}{c_T^2} \right)$$

From (200) reflection first  $a_T$  can be obtained, while (002) gives

$c_T$ .

### Rhombohedral System:

The interplaner spacing of rhombohedral system,  $d_R$  is given

by:

$$\frac{1}{d_R^2} = \frac{(h^2 + k^2 + l^2) \sin^2 \alpha + 2(hk + kl + hl)(\cos^2 \alpha - \cos \alpha)}{a_R^2 (1 - 3 \cos^2 \alpha + 2 \cos \alpha)}$$

' $\alpha$ ' is the angle between 'b' and 'c' sides of the lattice and also  $a = b = c = a_R$ .

The lattice parameter determination using the above equation is tedious. Easier method of calculation is via hexagonal system.

If H,K,L, are Millers Indices in hexagonal system and h,k,l are of rhombohedral system then,

$$H = h-k, K = k-l, L = h + k + l.$$

Interplaner spacing of hexagonal system is given by,  $d_H$ , as

$$\frac{1}{d_H^2} = \frac{4}{3} \frac{H^2 + HK + L^2}{a_H^2} + \frac{L^2}{c_H^2} \quad [a_H = b_H = c_H]$$

where  $a_H$ ,  $c_H$  are sides of the crystal lattice.

Combining the above equation with Bragg's law, we get,

$$\sin^2 \theta = \frac{2}{4} \left[ \frac{4}{3} \left\{ \frac{H^2 + HK + L^2}{a_H^2} \right\} + \frac{L^2}{c_H^2} \right]$$

This equation can be solved for  $a_H$  and  $c_H$  by using data of any two rhombohedral peak position.

From the values of  $a_H$  and  $c_H$ ,  $a_R$  and  $\alpha$  can be calculated using the following equation:

$$a_R = \frac{1}{3} \left( 3a_H^2 + c_H^2 \right)^{1/2}$$

$$\text{and } \sin\left(\frac{\alpha}{2}\right) = \frac{\sqrt{3}}{2 \left[ 3 + \left( \frac{c}{a} \right)^2 \right]^{1/2}}$$

H      H

Subscripts T, R, H indicates tetrahedral, rhombohedral and hexagonal system respectively.

## 2.3 Measurement of Sintered Density

The sample was heated at 150°C for 30 minutes in an oven to remove the moisture present in it. The dry weight ( $W_1$ ) of the sample was taken by a digital balance.

It was then kept in boiling water for 1 hour and 30 minutes. After cooling to room temperature it was weighed under water ( $W_2$ ). Then,

$$\text{Density} = \frac{W_1}{W_1 - W_2}$$

## 2.4 Measurement of Piezoelectric Properties

It was mentioned earlier that virgin ferroelectric material gives rise to isotropic property due to random orientation of the ferroelectric domains. Hence to develop the piezoelectric properties in it the ferroelectric domains should be aligned in a particular direction under the action of electric field. The process by which it is done is known as 'poling'.

### 2.4.1 Poling

During the cooling from high temperature paraelectric state to ferroelectric state each unit cell of the ceramic gets

44

deformed and lengthen in the direction of polar axis. This results in high intergranular stress. To minimise this stress ferroelectric domains form. Polarisation direction of domains are basically high temperature symmetry axes,  $\langle 001 \rangle$ ,  $\langle 110 \rangle$  and  $\langle 111 \rangle$ ; and angle between domains are  $90^\circ$ ,  $180^\circ$ ,  $71^\circ$  etc. [45]. Under the action of electric field the polar axes of the domains try to align themselves nearest to the field direction permitted by symmetry considerations. It is impossible to align all the polar axes in the same direction because of initial random orientation of domains. Baerwald [46] on the basis of random orientation of domains calculated the fraction of polarisation in orthorhombic phase having  $[110]$  as polar axis to be 91.2%. In another paper R. Redin et al [47] showed this percentage for tetragonal phase and rhombohedral phase to be 83% and 91% respectively. Once poled, the polycrystal ceramic acts much like a single crystal with the whole body acting as a single entity.

Strong electric field is required for poling and it may be continuous or intermittent or even varying in strength [48]. The dielectric strength of air is very low. Hence media of higher dielectric strength is needed in which poling can be performed safely. Required poling field and time decrease with increasing temperature. Generally poling is performed at about  $100^\circ\text{C}$  [49]. Time of poling varies from as low as 5 minutes to even hours. After poling of certain fixed time the material is cooled to room temperature with field on.

Gerson and Marshall [50] gave an empirical relation for the effect of thickness on break down field for  $\text{Pb}(\text{Zr},\text{Ti})\text{O}_3$  system

$$E = 27.2 t^{-0.39}$$

where,

$t$  = thickness in cm

$E$  = breakdown field in kV/cm.

Determination of ideal poling condition is a difficult task as it depends on many parameters like,

- i) Grain size, and size distribution
- ii) Strength of the ceramic
- iii) Amount of different phases present
- iv) Precipitation of any second phase in the grain boundary
- v) Thickness of the sample
- vi) Temperature of the environment
- vii) Poling field
- viii) Poling time

#### 2.4.2 Sample Size and Shape

The sample size and shape is an important parameter for measurement of piezoelectric properties. If in the disk shaped sample the thickness to diameter ratio ( $t/d$ ) is less than 0.1, then the error will be less than 1 percent [51]. For rectangular bar shaped specimen square of length to thickness ratio  $(l/t)^2$  and length to width ratio  $(R/w)^2$  should be greater than 10 [52]

In the present study measurements were restricted to disc shaped specimens only. The dimension of disc was  $t = 1$  mm and  $d = 12$  mm. The disc was polished on both surface with 0(0), 2(0), 3(0) and 4(0) emery papers to make the surfaces smooth and devoid of flaws which might cause dielectric breakdown.

#### 2.4.3 Poling Process

The disc were gold coated using INTERNATIONAL SCIENTIFIC INSTRUMENTS PS-2 COATING UNIT.

The coating conditions were as follows:

Current	=	10 mA
Voltage	=	1.1 - 1.3 kV
Pressure	=	0.1 - 0.2 torr
Atmosphere	=	Argon atmosphere
Time	=	12 minutes

A strong electric field was applied to the gold coated disk placed tightly between the two spring loaded electrodes using a fixture. The schematic diagram is shown in figure 2.2. To avoid dielectric breakdown the whole system was immersed in silicon oil bath. The poling field was along the thickness of the disk.

Following poling conditions were adopted:



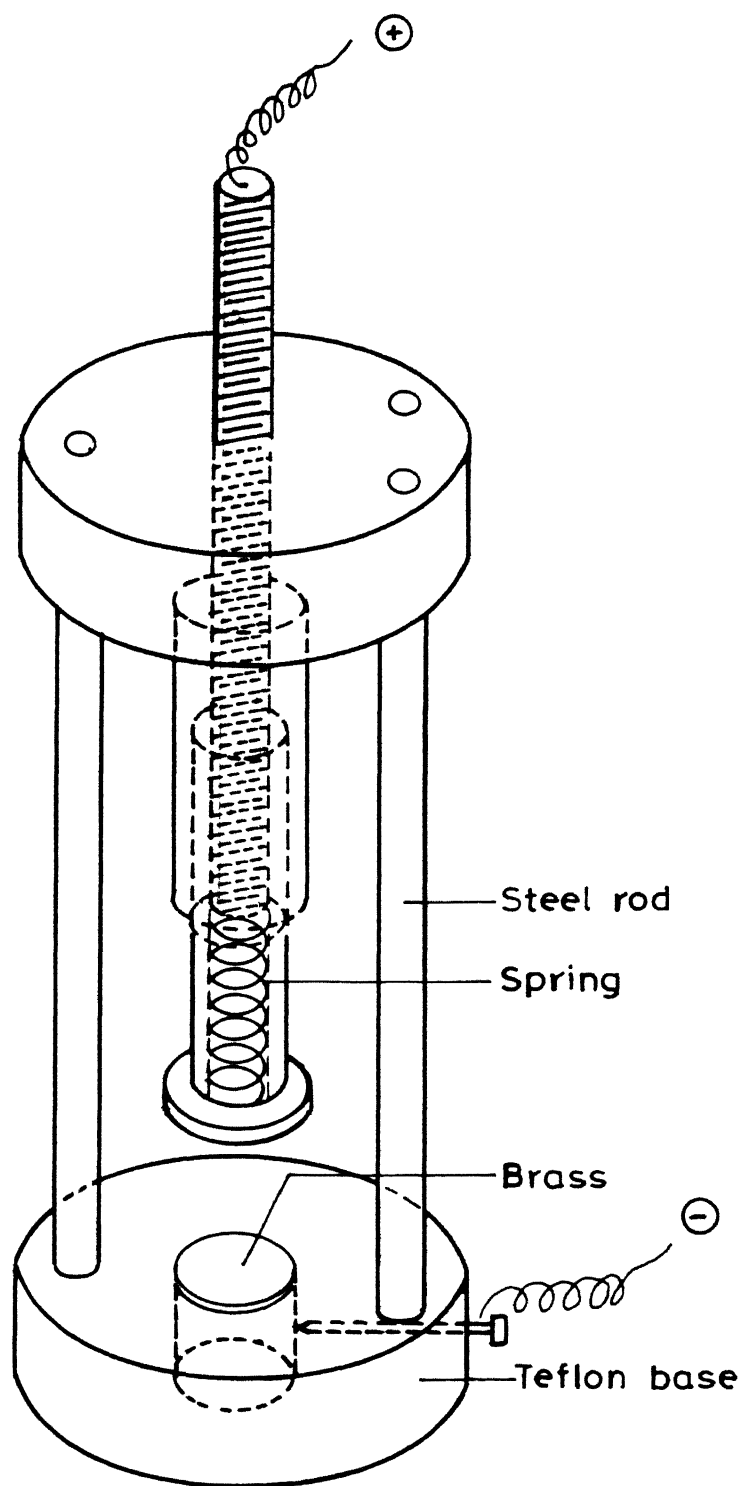


Fig.2.2 Schematic diagram of poling fixture .

Applied field

3.5 kV/mm

48

Temperature of oil bath

$100^{\circ}\text{C} \sim 120^{\circ}\text{C}$

Time

30 minutes in the temperature range  $100^{\circ}\text{C}$  to  $120^{\circ}\text{C}$ . Then cooled down with field on to  $60^{\circ}\text{C}$  in approximate 25 minutes, field switched off and cooled to room temperature.

#### 2.4.4 Measurement Techniques

Two types of techniques can be used:

- i) Static method
- ii) Dynamic method.

Piezoelectric constants may be measured by the techniques of static method with reasonable accuracy but the precision is inferior to that obtained with dynamic method. Hence the discussion is restricted to later method only.

Elastic bodies show numerous resonances. But the most pronounced are those where the body can just accommodate one half wavelength of a standing wave. Piezoelectric effect is used to excite such elastic wave and to observe interaction of the mechanical resonance with electric field behaviour.

## Resonance Method

This is a simple dynamic method for evaluating piezoelectric constants by measuring the resonant ( $f_r$ ) and antiresonant ( $f_a$ ) frequencies corresponding to a longitudinal mode by means of a simple electric circuit as shown in the figure (2.3).

When the piezoelectric material is put in the circuit, the electric field sets up vibration in the material through direct piezoelectric effect. The commonly encountered modes of motion of bars, plates and disks excited piezoelectrically by electric field are

- i) Length extentional mode
- ii) Over tone contour-shear mode
- iii) Contour extentional mode
- iv) Contour mode
- v) Contour extentional mode (disk)

The first two modes of motion are for narrow bars, third and first correspond to square plate and the last mode of motion is for disk.

The periodic vibration of the crystal causes periodic piezoelectric changes on the electrode through converse effect. The properties of any mode of a lightly-damped mechanical vibrating system (excited piezoelectrically) can be represented near resonance by an equivalent electric circuit (fig. 2.4) which consist of a capacitance  $C_1$ , inductance  $L_1$ , and resistance  $R_1$ , in series, shunted by a second capacitance  $C_o$  in parallel. These are the fundamental parameters of the piezoelectric vibrator.

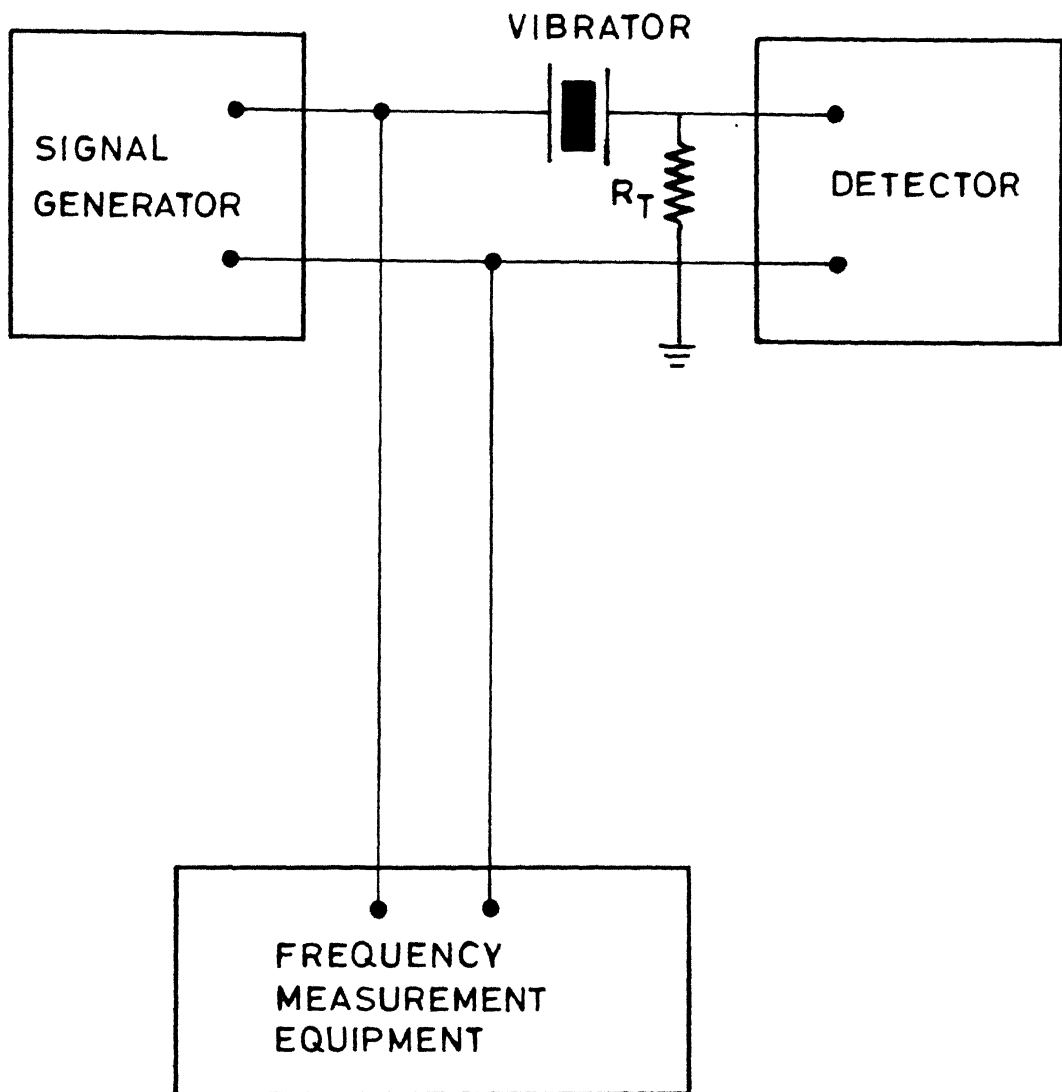


Fig. 2.3 Transmission net work for determination of  $f_r$  and  $f_a$  of piezoelectric ceramic vibrator.

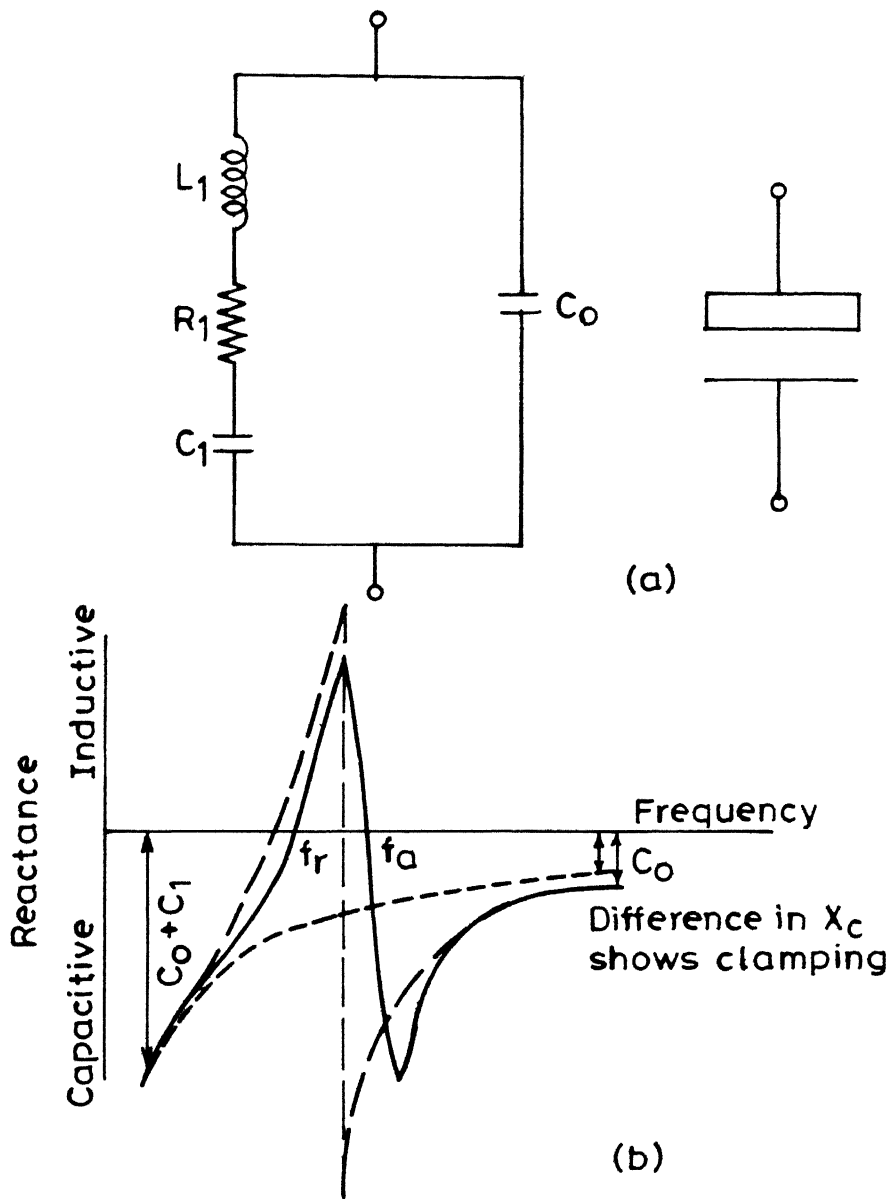


Fig.2.4 (a) Equivalent circuit of a piezoelectric body  
 (b) Reactance of piezoelectric resonator. [5]

The parameters are independent of frequency if the vibrator has no other mode of motion near resonance.

The equivalent series resistance and reactance of the R L C C circuit is given by

$$R_s = \frac{R_1}{[1 - \omega^2 C_1^2 X_1^2] + \omega^2 C_1^2 R_1^2}$$

$$X_s = \frac{X_1 - \omega^2 C_1^2 [R_1^2 + X_1^2]}{[1 - \omega^2 C_1^2 X_1^2] + \omega^2 C_1^2 R_1^2}$$

where  $X_1 = \omega L_1 - \frac{1}{\omega C_1}$ , reactance of the  $R_1, L_1, C_1$  branch in the series. The resonance frequencies are obtained by setting  $X_s = 0$ . At resonance  $R$  is nearly zero.

Solving this series resonance,  $f_s$ , is given by

$$f_s = \frac{1}{2\pi(L_1 C_1)^{1/2}}$$

Similarly parallel resonance can be obtained as

$$f_p = \frac{1}{2\pi} \left[ \frac{C+C_0}{L} \right]^{1/2}$$

Variation of series reactance,  $X_s$ , with frequency is shown in figure 2.4b. The frequencies at zero reactance are measured. Piezoelectric properties are measured using their resonant  $f_r$  (minimum impedance) and antiresonance  $f_a$  (maximum impedance) frequencies. Complete scheme of measurements are given in Appendix 1 [51].

Here the measurements are restricted to disk shaped samples only  $f_r$  and  $f_a$  are measured by using 4194A IMPEDANCE/GAIN PHASE ANALYSER (HEWLETT-PACKARD).

Planer coupling coefficient  $K_p$ , is obtained from the  $f_r$  and  $f_a$  values of the thin disk with faces perpendicular to z-axis as follows:

$$K_p^2 = \frac{(1 - \sigma_1) J_1^2 \left[ \eta_1 \left( 1 + \frac{\Delta f}{f_r} \right) \right] - \eta_1^2 \left( 1 + \frac{\Delta f}{f_r} \right) J_0^2 \left[ \eta_1 \left( 1 + \frac{\Delta f}{f_r} \right) \right]}{(1 + \sigma_1) J_1^2 \left[ \eta_1 \left( 1 + \frac{\Delta f}{f_r} \right) \right]}$$

where

$J$  = Bessel function of first kind and zero order

$J_1$  = Bessel function of first kind and first order

$\eta_1$  = Lowest positive root of  $(1 + \sigma^E) J_1 = \eta_0 J_0(\eta)$

For  $\sigma^E = 0.3$  (poisson ratio),  $\eta_1 = 2.05$ .

The relationship is plotted in fig. 2.5 where  $k$  is shown <sub>P</sub>

as a function of  $\Delta f/f$  curve is for  $\sigma^E = 0.3$  [51].  
<sub>r</sub>

$k_{33}$  and  $k_{31}$  are calculated as follows:

$$k_{33}^2 = \frac{\pi}{2} \frac{f}{a} \tan\left(\frac{\pi}{2} \frac{\Delta f}{f}\right)$$

$$k_{31}^2 = \left( \frac{1 - \sigma^E}{2} \right) k_p^2$$

$d_{33}$  was measured by using the CHANNEL PRODUCTS, MODEL CPDT 3300

BERLIN COURT PIEZO  $d_{33}$  METER,

$d_{31}$  is calculated as follows:

$$d_{31} = k_{31} (\epsilon_{33}^T \epsilon_{11}^E)^{1/2} \quad \text{Coulombs/Newton}$$

where,

$$\frac{1}{s^E} = \frac{\pi^2 d^2 f^2 (1 - \sigma^E)^2 \rho}{\eta^2}$$



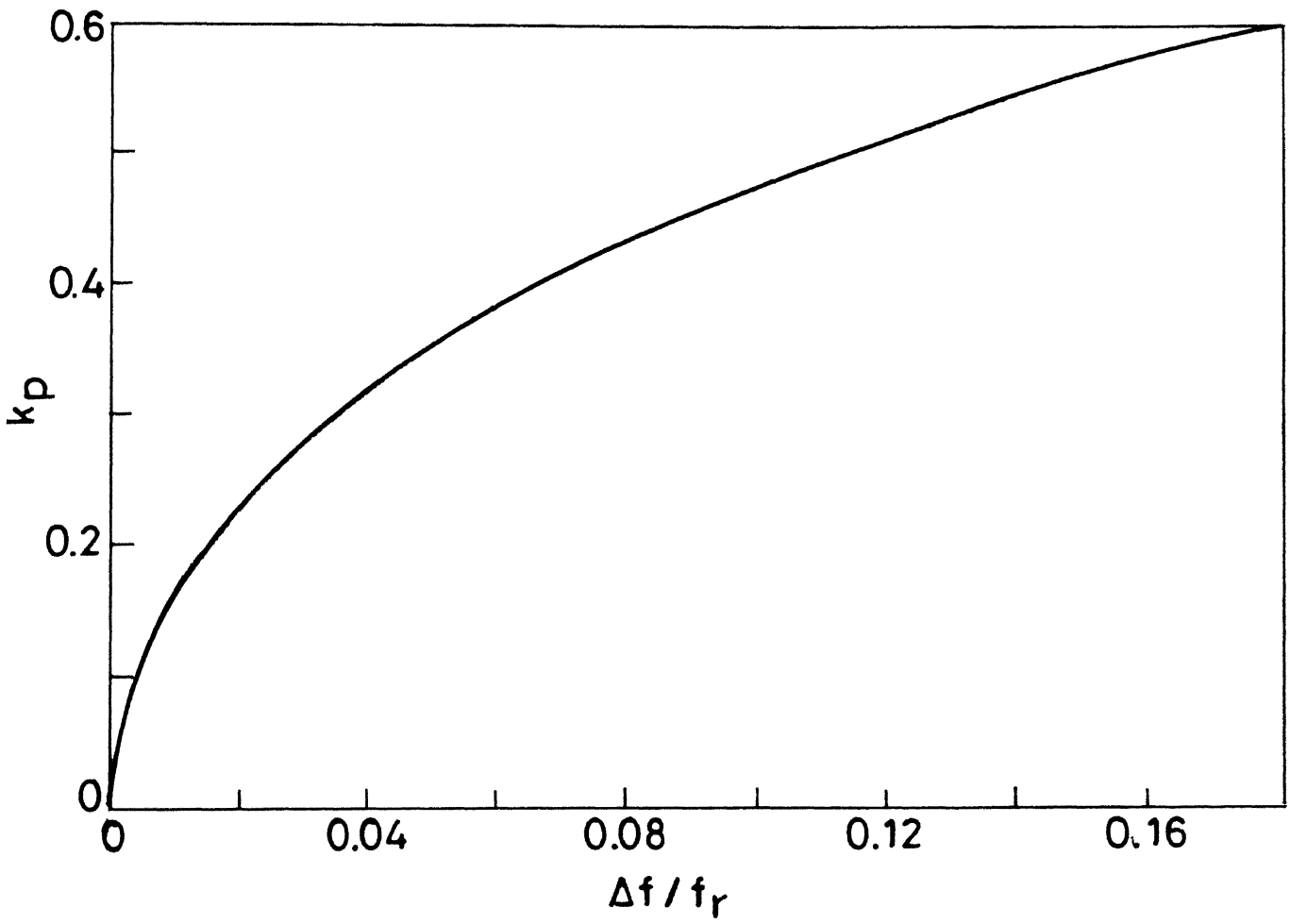


Fig. 2.5 Planar coupling factor of thin disk .[51]

$\rho$  = density of disk

$\eta$  = 2.05

$\sigma^E$  = 0.29 ~ 0.33

$\epsilon_{33}^T$  - free dielectric constant, obtained as shown later.

$K_{33}^T$  is given by

$$K_{33}^T = \frac{d_{33} \text{ Volt-meter}}{\epsilon_{33}^T \text{ Newton}}$$

$K_{33}^S$  (relative clamped dielectric constant, longitudinal) is calculated as:

$$K_{33}^S = \frac{C \times t}{A \times 0.0085}$$

$C$  = capacitance in picofarad

$t$  = thickness in cm

$A$  = area in cm

$$\epsilon_{33}^T = K_{33}^T \times 8.54 \times 10^{-12} \text{ farad/meter.}$$

$K_{33}^T$  (relative free dielectric constant) is calculated from  $K_{33}^S$  by  
by

$$K_{33}^T = \frac{K_{33}^S}{1 - K_p^2}$$

Poled samples are cleaned thoroughly with acetone and again gold coated for five minutes to restore the continuity on the both surface. The samples were put in a similar fixture used for

poling for further analysis. The measurements were done 24 hours after poling to allow for the 'aging' to take place.

The measurements were done on first a disk shaped test sample supplied by American Piezo Ceramics Inc. Mackeyville, PA17750 USA. The results showed the good accuracy of the measurement technique.

## 2.5 Measurements of Mechanical Properties

### 2.5.1 Vickers Hardness

The samples were cylindrical and 6 mm thick. One of the two flat surfaces was polished successively on 0(0), 2(0), 3(0) and 4(0) grade emery polishing papers. Final polishing was done by lapping on polishing wheel with 0.3 micron alumina powder.

Indentations were carried out on a Vicker's testing machine having a load range 2.5 kg to 30 kg. The load depended on the hardness of the sample is being smaller for softer samples. The load was selected so as to give an indentation which was not too large, but at the same time could be easily measured. The average length of diagonals were measured by the microscope attached with the instrument.

Vickers Hardness Number ( $H_V$ ) was calculated using the formula (55)

$$H_V = \frac{1.8544 P}{(2a)^2}$$

where P is load in kg and (2a) is the average diagonal in mm.

### 2.5.2 Modulus of Rupture

Modulus of rupture (MOR) was determined using a four-point bending fixture (fig. 2.6) on an INSTRON-1195 system. The samples for this test were prepared by cutting pieces of approximate size of 18x4x2 mm. These pieces were polished in the same manner as for Vickers Hardness testing. The sample configuration is shown in figure 2.7.a. Following experiments parameters were used:

Span (L)	=	10 mm
Width of sample	—	4 mm
Depth of sample	—	2 mm
Cross head speed	=	0.05 mm/min
Chart speed	=	50 mm/min
Load cell	=	1000 kg max.
Full scale load	=	0.2 K Newton

Load at fracture was determined for each test specimen. MOR is calculated by the following formula [54]

$$\text{MOR} = \frac{3 \cdot P \cdot a}{bh^2} \times 9.806 \text{ MPa}$$

a = The distance from the support to the load applicator when specimen is straight

b = Specimen width

h = Specimen thickness

where P is in kg and 'a', 'b', and 'h' in mm.

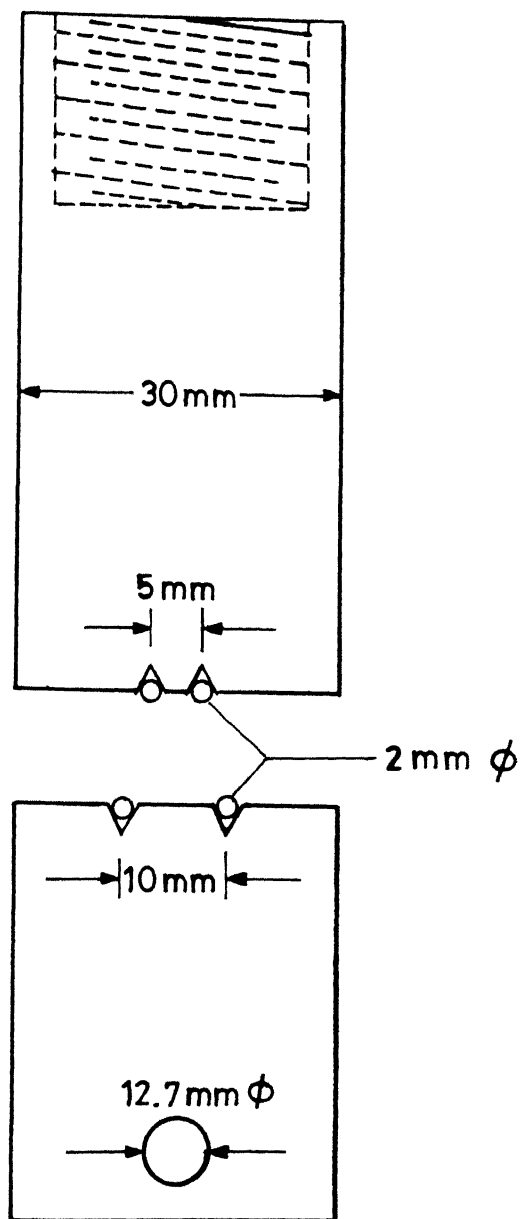


Fig.2.6 Four point bending fixture

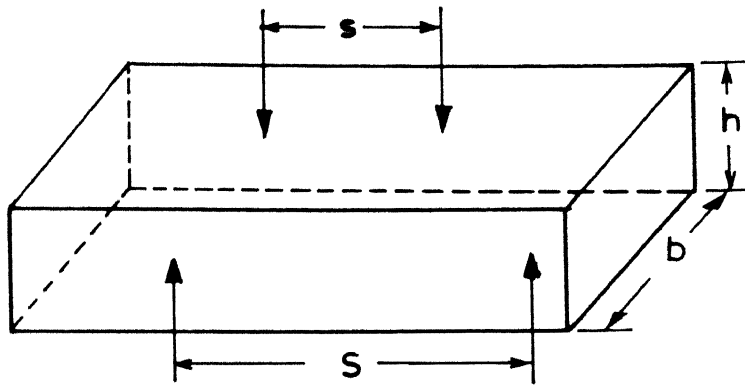


Fig.2.7 (a) Specimen configuration for MOR and Youngs modulus test.

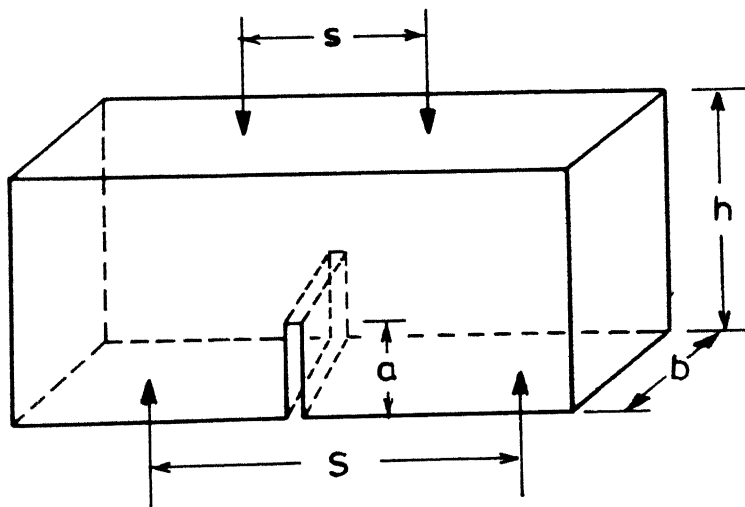


Fig.2.7 (b) Specimen configuration for  $K_{IC}$  test

### 2.5.3 Young's Modulus

The load obtained in MOR test was utilised to calculate the Young's Modulus. The central deflection of the beam was calculated from the load-displacement chart. Error in the central deflection was corrected by subtracting the deflection due to the machine. The deflection of the machine was found out by using a dummy specimen (large iron piece) whose Young's modulus is much higher than the materials under test.

The dimension of dummy specimen was

Length        20 mm

Width        = 8 mm

Depth        = 4 mm

The following formula was used to calculate the Young's Modulus [54].

$$E = \frac{P \cdot a (3L^2 - 4a^2)}{4 b h^3 \delta}$$

L        span length between the supports

b        specimen width

h        specimen thickness.

P        Load

$\delta$         Deflection at the mid-span

a        The distance from the support to the load applicator when the specimen is straight

P        in kg; a, L, b, h,    in mm.

## 2.5.4 Fracture Toughness

'Single edge notch beam' method was used to determine the fracture toughness for the present investigation.

The samples were cut with approximate dimension 18x4x2 mm and were polished as discussed in Vicker's Hardness Measurement. The notches were made using diamond edge blade of 0.4 mm thickness. The notch length varied between 0.8 mm to 1.5 mm. Accurate measurement of notch length was done by travelling microscope. The sample configuration is shown in figure 2.7b. The samples were broken in four point bending fixture using INSTRON 1195 system with following experimental parameters:

Span length	=	10 mm
Cross head speed	=	0.05 mm/min
Chart speed	=	50 mm/min
Load cell	=	1000 kg (max. limit)
Full scale load	=	0.2 kN.

The following formula was used to calculate  $K_{IC}$  [55]:

$$K_{IC} = \frac{3 P d^2 a^{1/2}}{b h^2 [3.86 - 6.15(a/h) + 21.7(a/h)^2]^{1/2}}$$

where

$$d = \frac{S-s}{2}$$

$$b = \text{Breadth of sample}$$



$h$  = Depth of sample

$a$  = Notch length

$P$  is in Newton,  $a, d, b, h$  are in meter.

## 2.6 Microstructure Analysis

Fracture surface of the PZT samples were observed using JSM 840A SCANNING MICROSCOPE, JEOL.

The sample was broken before putting it in the microscope and was cleaned thoroughly using ultrasonic vibrator. Then it was gold coated for one minute thirty second.

## CHAPTER - III

### RESULTS AND DISCUSSION

#### 3.1 Phase Analysis

$\text{Pb}(\text{Zr}_{1-x}\text{Ti}_x)\text{O}_3$  perovskite solid solution depending on the composition can exist in any one of the three structures, Tetragonal (T) ( $0 \leq x \leq 0.52$ ), Rhombohedral (R) ( $0.52 \leq x \leq 0.92$ ) and Orthorhombic (O) ( $0.92 \leq x \leq 1.0$ ) [5] with sharp boundaries between tetragonal and rhombohedral phases which is known as Morphotropic Phase Boundary (MPB). The existence of a constant composition morphotropic phase boundary has been contradicted by many researchers [12,56,57,58]. They suggested that tetragonal and rhombohedral phases coexist in the transition with some range of compositions. These authors got different results regarding the width of the coexistence region.

In the present work both the phases are found to be present in the undoped sintered material [Fig. 3.1]. In the calcined samples both the phases are present for  $\text{CeO}_2$  content upto 2

mole% while at 5 mole%  $\text{CeO}_2$  only the tetragonal phase is present

as shown by slow scan ( $0.6^\circ/\text{minute}$ ) between  $2\theta = 43^\circ$  to  $46^\circ$  (fig. 3.2). In the sintered sample orthorhombic phase is found to coexist with the tetragonal phase only upto 0.1 mole percent  $\text{CeO}_2$

(fig. 3.3). Three different  $2\theta$  ranges are shown in this figure where the disappearance of the rhombohedral phase with increasing  $\text{CeO}_2$  can be clearly observed. Free  $\text{CeO}_2$  is present in 5 mole%  $\text{CeO}_2$  sample (fig. 3.4).

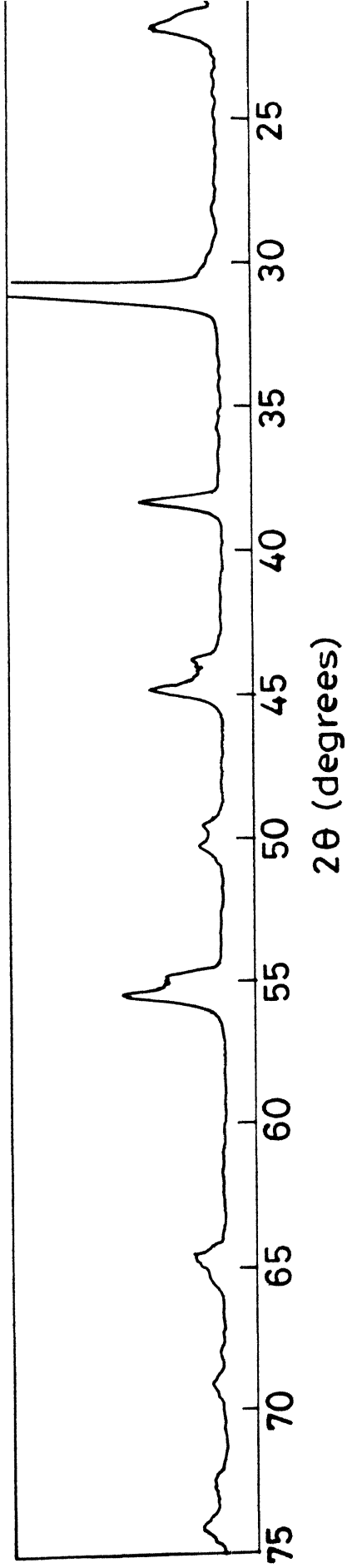


Fig.3.1 Slow scan XRD - pattern of PZT ( $x = 0.535$ )

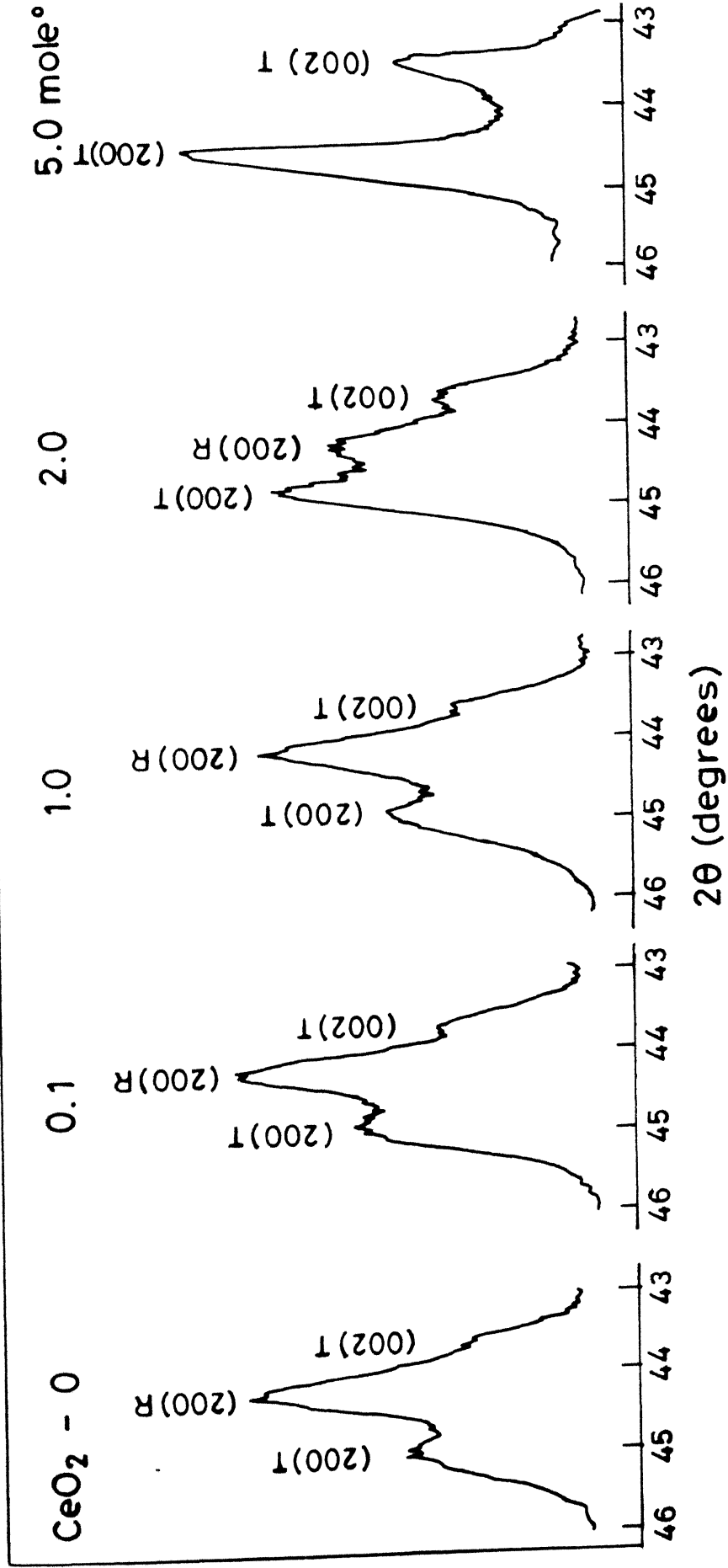


Fig. 3.2 Slow scan XRD-pattern of calcined PZT powders with CeO<sub>2</sub> varying from 0 - 5.0 mole % .

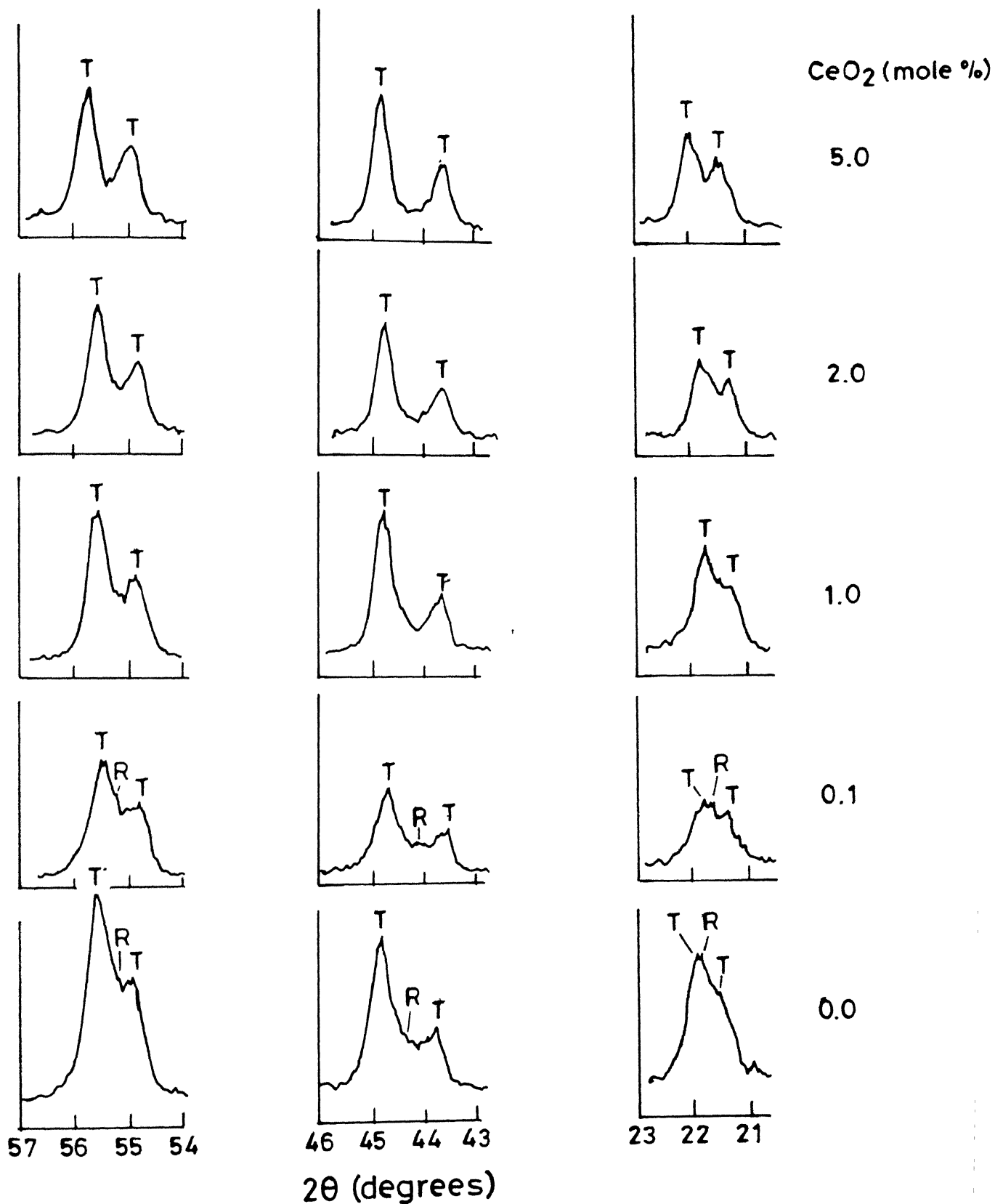


Fig.3.3 Details of slow scan XRD patterns of sintered samples.

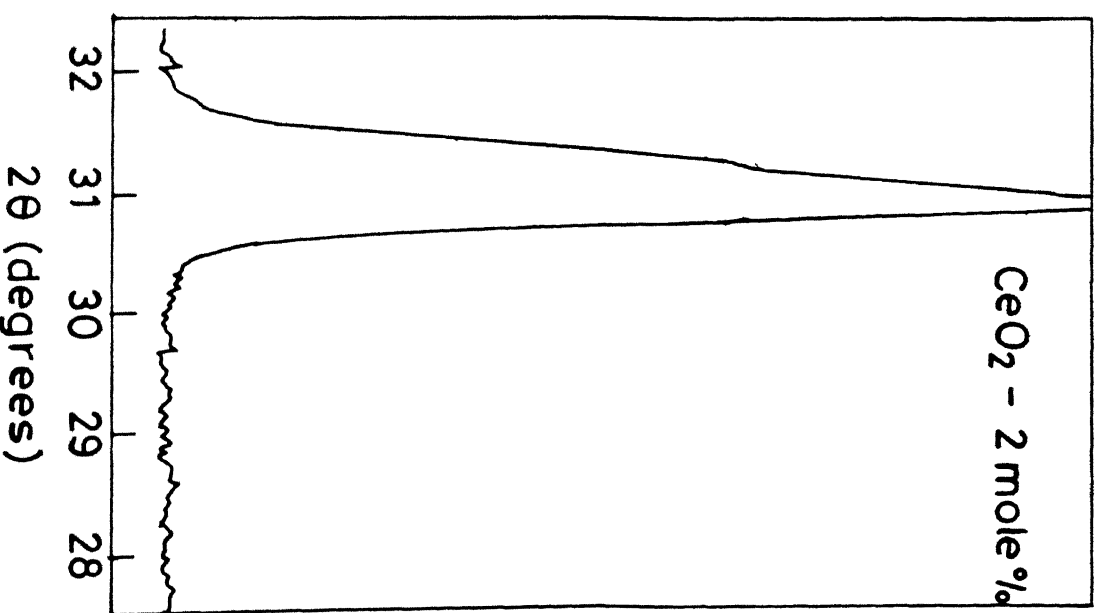
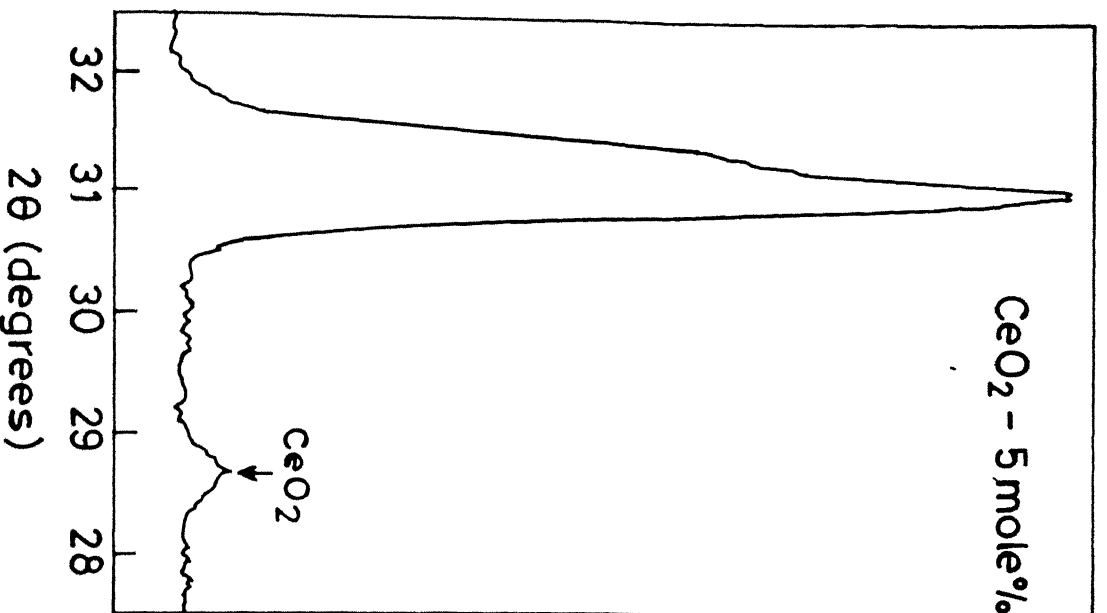


Fig.3.4 Free  $\text{CeO}_2$  is present only at the highest  $\text{CeO}_2$  content of 5 mole % .

The values of lattice parameter  $a_T$  and  $c_T$  for tetragonal phase and  $c/a_T$  ratios are given in table 3.1

Table 3.1  
Lattice Parameters for Tetragonal Phase in PZT

Concentration of CeO <sub>2</sub> % (mole percent)	$2\theta$ for (002) plane	$2\theta$ for (200) plane	$c_T$ in Å	$a_T$ in Å	$c/a_T$
0%	43.83	44.88	4.1276	4.0357	1.0227
0.1%	43.76	44.82	4.1337	4.0408	1.0229
1.0%	43.72	44.80	4.1373	4.0425	1.0234
2.0%	43.69	44.86	4.1398	4.0374	1.0253
5.0%	43.74	44.96	4.1355	4.0289	1.0264

It is known that as 'x' decreases, the rhombohedral phase disappears near MPB and its content decreases with decreasing 'x'. Also the  $c/a$  ratio for the tetragonal phase decreases as x increases.

Replacement of  $ZrO_2$  by  $CeO_2$  in this work implies lower  $ZrO_2$  content for increasing amount of  $CeO_2$ . One interpretation of these results could be that  $CeO_2$  is acting as an inert phase and the observed results are solely due to the changing concentration of zirconia.

However, it is more likely that at least some  $CeO_2$  has entered the PZT lattice. Thus the EDAX analysis of the samples

show  $\text{CeO}_2$  to be present through out all the grains. As discussed later, second phase particles appear at grain boundaries at 5 mole %  $\text{CeO}_2$  and to a lesser extent for 2 mole %  $\text{CeO}_2$ . Thus it appears that  $\text{CeO}_2$  is dissolving in the PZT lattice to a limited extent possibly upto 1 mole %  $\text{CeO}_2$ .

EDAX analysis at a spot on a very small grain in the grain boundary of the larger grains shows the peak of  $\text{Ce}^{+4}$  ion be appreciably large compared to  $\text{Ti}^{+4}$  and nearly equal to  $\text{Zr}^{+4}$ . As the analysis was performed on the fractured surface and the influence of the nearby regions of the other grains might be high the result obtained by this analysis is not accurate enough. But qualitatively it can be ascertained the small particles at the grain boundaries to be ceria which is again supported by X-ray result atleast for 5 mole %  $\text{CeO}_2$ .

### 3.2 Sintered Density

Sintered density of the five sets of PZT compositions are shown in table 3.2. Their variation with the doping concentration is shown in figure 3.5. It is observed that sintered density is maximum to undoped PZT. Minimum value is obtained at doping concentration of 1.0 mole %  $\text{CeO}_2$ . Beyond this the sintered density again increases with increasing doping concentration.



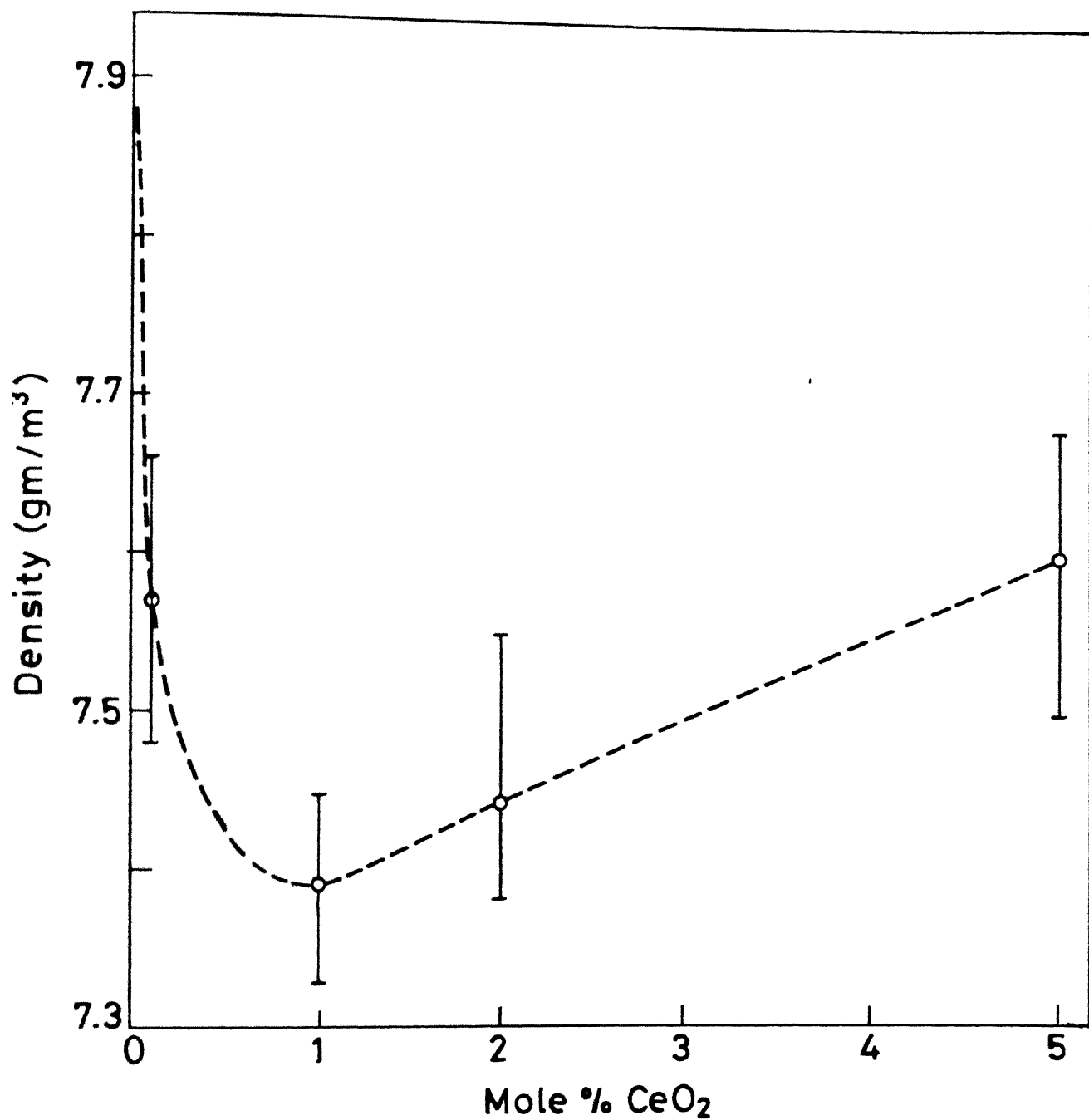


Fig. 3.5 Variation of density with concentration of ceria.

Table 3.2

## Density of Ceria Doped PZT Ceramics

Doping concentration of $\text{CeO}_2$ in mole %	Range of sintered density gm cm <sup>-3</sup>	Mean value of sintered density gm cm <sup>-3</sup>
0.0	7.84 - 7.94	7.88
0.1	7.48 - 7.63	7.57
1.0	7.33 - 7.45	7.39
2.0	7.38 - 7.55	7.44
5.0	7.50 - 7.68	7.60

## 3.3 Piezoelectric Properties

The variation of reactance with frequencies for test sample obtained from American Piezo Ceramics Inc. Mackeyville, PA17750, USA and some of the PZT disks of different composition are shown in figure 3.6. All the samples responded well to the impedance analyser. The values of resonant and antiresonant frequencies are listed in table 3.3

Table 3.3

## Range of Resonant and Antiresonant Frequencies

Concentration of $\text{CeO}_2$ in PZT (mole %)	Range of resonant frequencies ( $f_r$ ) (Hz)	Range of antiresonant frequencies ( $f_a$ ) (Hz)
0	163000 - 165540	176500 - 179120
0.1	162175 - 163250	176875 - 178250
1.0	172600 - 173785	180995 - 181350
3.0	174900 - 177680	181600 - 186050
5.0	185192 - 191200	187450 - 192900

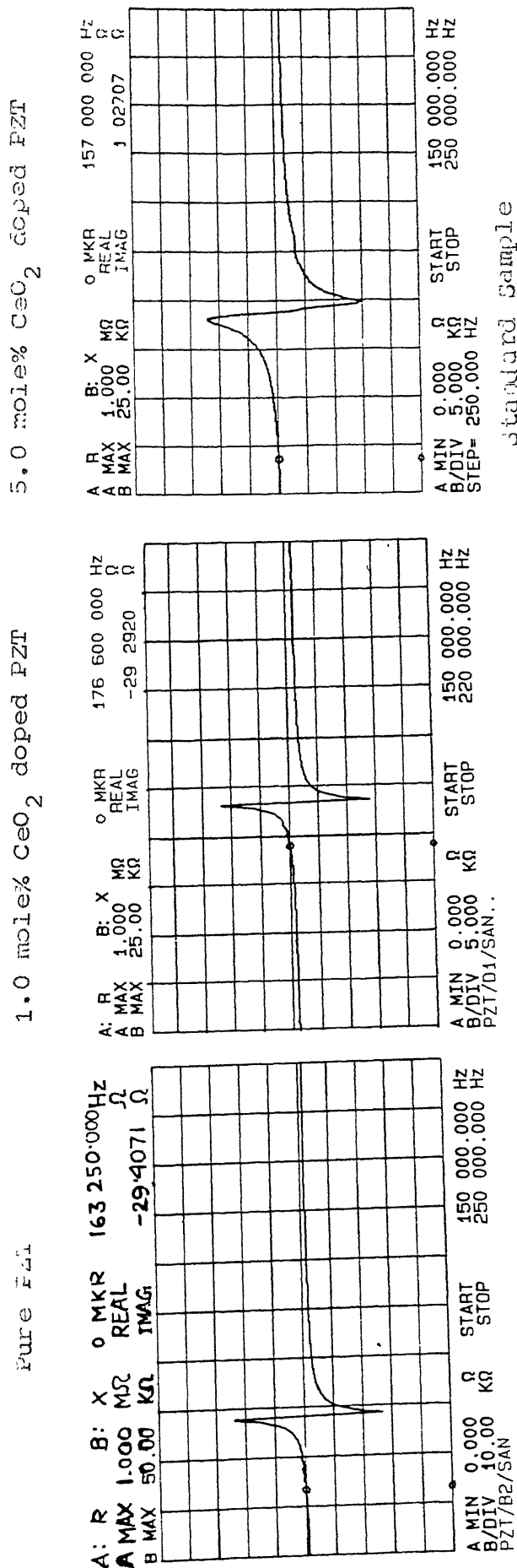
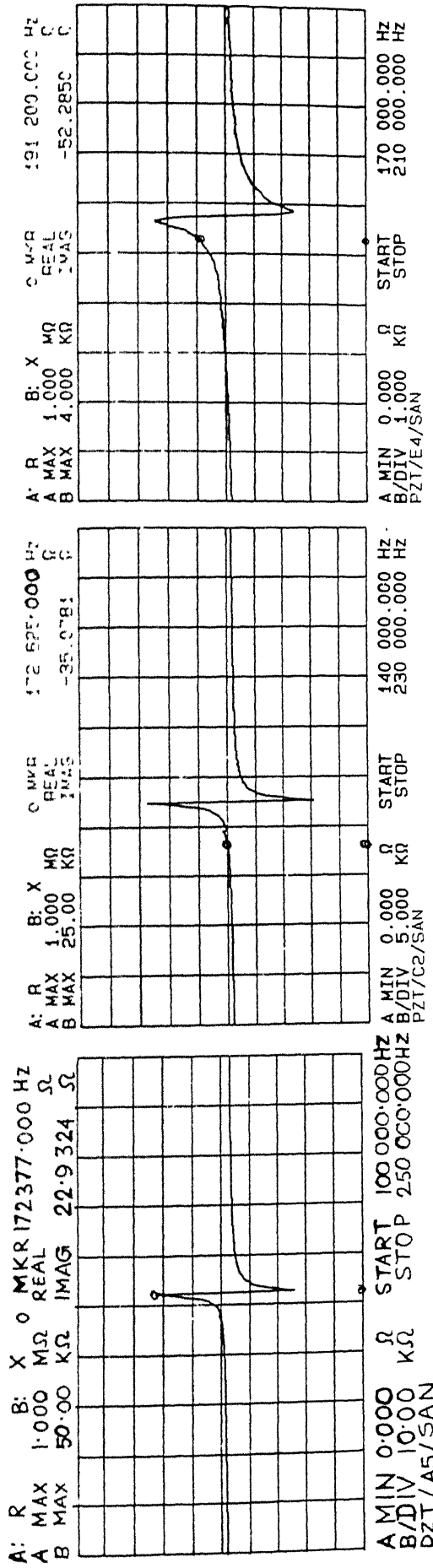


Fig 3.6 : Variation of Reactance with Frequency

Values of capacitance as obtained by the impedance analyser are listed in table 3.4.

Table 3.4

Range of Capacitance of the PZT Samples at 100 KHz Frequency

Concentration of $\text{CeO}_2$ in PZT samples (mole %)	Range of capacitance in picofarad
0.0	595 - 701
0.1	791 - 830
1.0	914 - 977
2.0	890 - 954
5.0	738 - 796

Free relative dielectric constant ( $K_{33}^T$ ), elastic compliance  
at constant electric field ( $S_{11}^E$ ), electromechanical coupling  
coefficients ( $k_p$ ,  $k_{31}$ ,  $k_{33}$ ) longitudinal voltage coefficient  
( $g_{33}$ ), strain coefficient ( $d_{31}$ ,  $d_{33}$ ) are calculated and the  
results are given in tables 3.5, 3.6, 3.7, 3.8 and 3.9  
respectively. The corresponding curves are shown in the figures  
3.7 to 3.11 respectively.

Table 3.5

Dielectric Constant of Ceria Doped PZT Ceramics at 100 KHz Frequency

Doping concentration of $\text{CeO}_2$ (mole %)	Range of $K^T$ 33	Average $K^T$ 33
0.0	767 - 899	804
0.1	1053 - 1104	1083
1.0	1058 - 1131	1084
2.0	1030 - 1104	1056
5.0	765 - 825	793

Table 3.6

Elastic Compliance of Ceria Doped PZT Ceramics

Doping concentration of $\text{CeO}_2$ (mole %)	Range of $S^E$ 11 ( $10^{-12} \text{ m}^2/\text{N}$ )	Average of $S^E$ 11 ( $10^{-12} \text{ m}^2/\text{N}$ )
0.0	14.94 - 15.41	15.14
0.1	16.13 - 16.34	16.23
1.0	14.62 - 14.82	14.75
2.0	14.18 - 14.34	14.26
5.0	11.66 - 12.30	12.18

# Electromechanical Coupling Coefficients of Ceria Doped PZT Ceramics

Doping concentration of $\text{CeO}_2$ (mole %)	$k_p$	Range of $k_{33}$	Average $k_{33}$	$k_{31}$
0	0.43	0.435-0.416	0.427	0.262
0.1	0.46	0.454-0.457	0.455	0.278
1.0	0.33	0.313-0.345	0.326	0.201
2.0	0.32	0.298-0.312	0.306	0.191
5.0	0.17	0.147-0.228	0.172	0.113

Table 3.8

## Voltage Coefficient of Ceria Doped PZT Ceramics

Doping concentration of $\text{CeO}_2$ (mole %)	Range of $g_{33}$ -3 (10 <sup>-3</sup> V-m/N)	Average $g_{33}$ -3 (10 <sup>-3</sup> V-m/N)
0	29.27 - 34.34	31.56
0.1	26.71 - 31.49	29.37
1.0	13.56 - 16.30	15.06
2.0	14.53 - 18.49	16.25
5.0	11.39 - 15.38	13.81

Table 3.9  
Strain Coefficients of Ceria Doped PZT Ceramics

Doping concentration of $\text{CeO}_2$ (mole %)	Range of $d_{33}$ ( $10^{-12}$ C/N)	Average $d_{33}$ ( $10^{-12}$ C/N)	Range of $d_{31}$ ( $10^{-12}$ C/N)	Average $d_{31}$ ( $10^{-12}$ C/N)
0.0	204.20-233.24	222.73	83.45- 91.00	86.01
0.1	261.11-293.38	278.78	107.80-111.10	109.67
1.0	135.79-152.74	144.06	74.68- 72.21	75.62
2.0	138.35-168.70	148.98	68.81- 71.24	69.68
5.0	80.84-112.83	93.46	31.76- 34.0	33.04

Free relative dielectric constant (figure 3.7) shows a definite improvement over pure PZT ( $x = 0.535$ ) at 0.1 mole %  $\text{CeO}_2$  doping. With increasing  $\text{CeO}_2$  concentration it remains constant and decrease slightly at 2.0 mole%  $\text{CeO}_2$  doping. Beyond this it falls drastically and at 5 mole percent  $\text{CeO}_2$  it becomes lower than pure PZT.

Elastic compliance ( $S_{11}^E$ ) is maximum at doping concentration of 0.1 mole %  $\text{CeO}_2$ . The peak values of  $K_p$ ,  $K_{33}$ ,  $K_{31}$  are also at doping concentration of 0.1 mole % and falls gradually with higher ceria content.

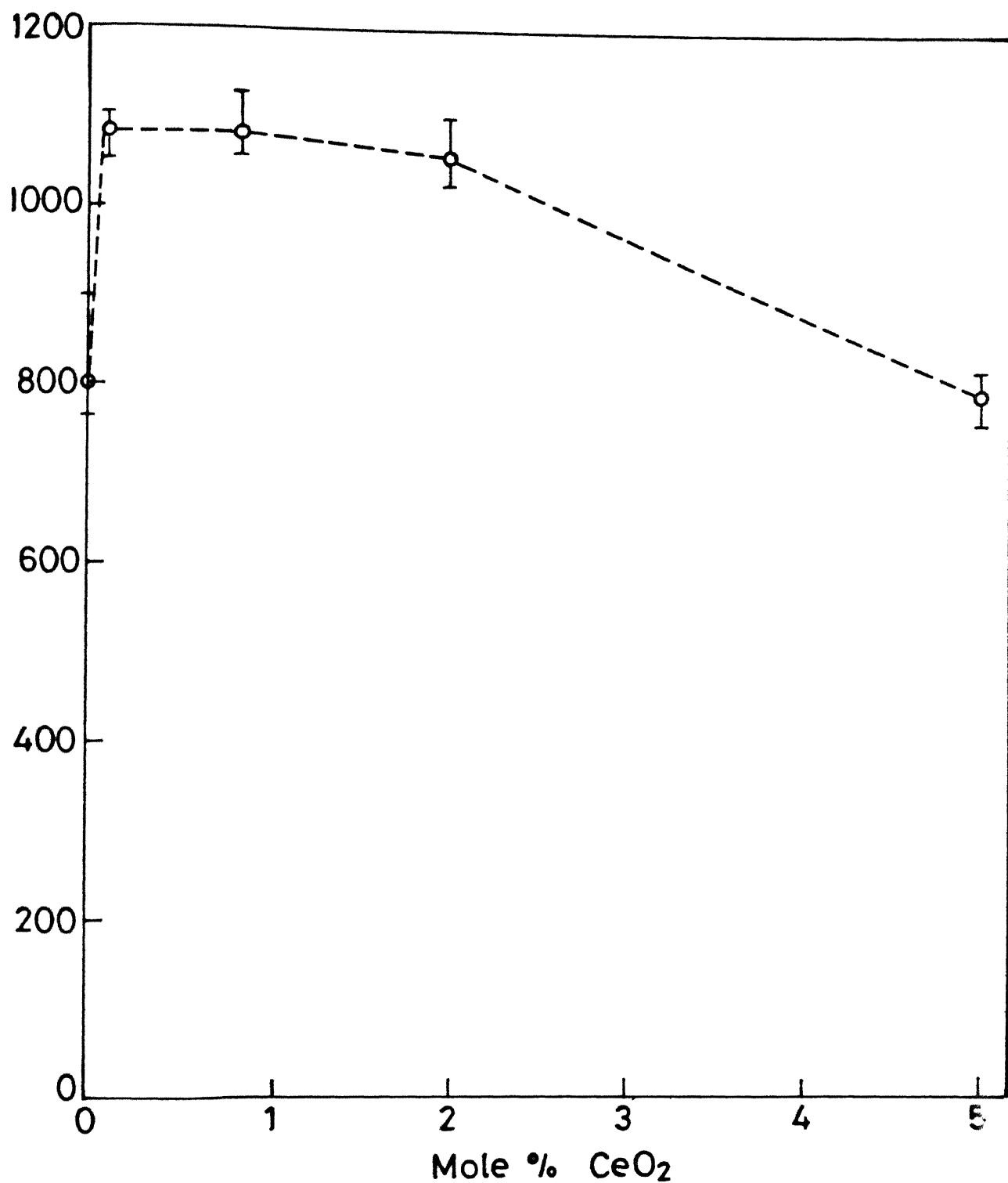
Voltage coefficient is maximum for pure PZT and gradually reduces.

Strain coefficient changes in the same fashion as that of electromechanical coupling coefficient with maximum value at 0.1 mole % ceria. Thus best piezoelectric properties are obtained at the lowest ceria concentration (0.1 mole %). Higher concentration deteriorate the piezoelectric properties.

Piezoelectricity in the morphotropic region is much higher than either in the tetragonal or rhombohedral phase region. Many authors [59,60,61] associate this phenomena with increased mobility of domain walls and more easy reorientation of the polarisation in this region. Jaffe et al [65] found that just on the rhombohedral side of the MPB PZT ceramics shows higher values of coupling coefficients. The grain size is another important factor.  $k$  increases with increasing grain size provided there is no microcrack. But microcrack occurs during polling which introduces space charge. This reduces the values of coupling coefficients. The extent of microcracking increases with increasing  $c/a$  ratio.

The piezoelectric constants of our sample increase upon the first addition of  $\text{CeO}_2$  to 0.1 mole% and then decrease with further addition of ceria to 1 mole%. At 0 mole%  $\text{CeO}_2$  and 0.1 mole%  $\text{CeO}_2$ , both rhombohedral and tetragonal phases exist, though the amount of the rhombohedral phase is very small, as deduced from the low intensity of the X-ray peaks, for 0.1 mole%  $\text{CeO}_2$ . Thus the 0 mole%  $\text{CeO}_2$  composition is nearly in the middle of the MPB composition while the 0.1 mole %  $\text{CeO}_2$  corresponding to the





.3.7 Variation of free relative dielectric constant with concentration of ceria.

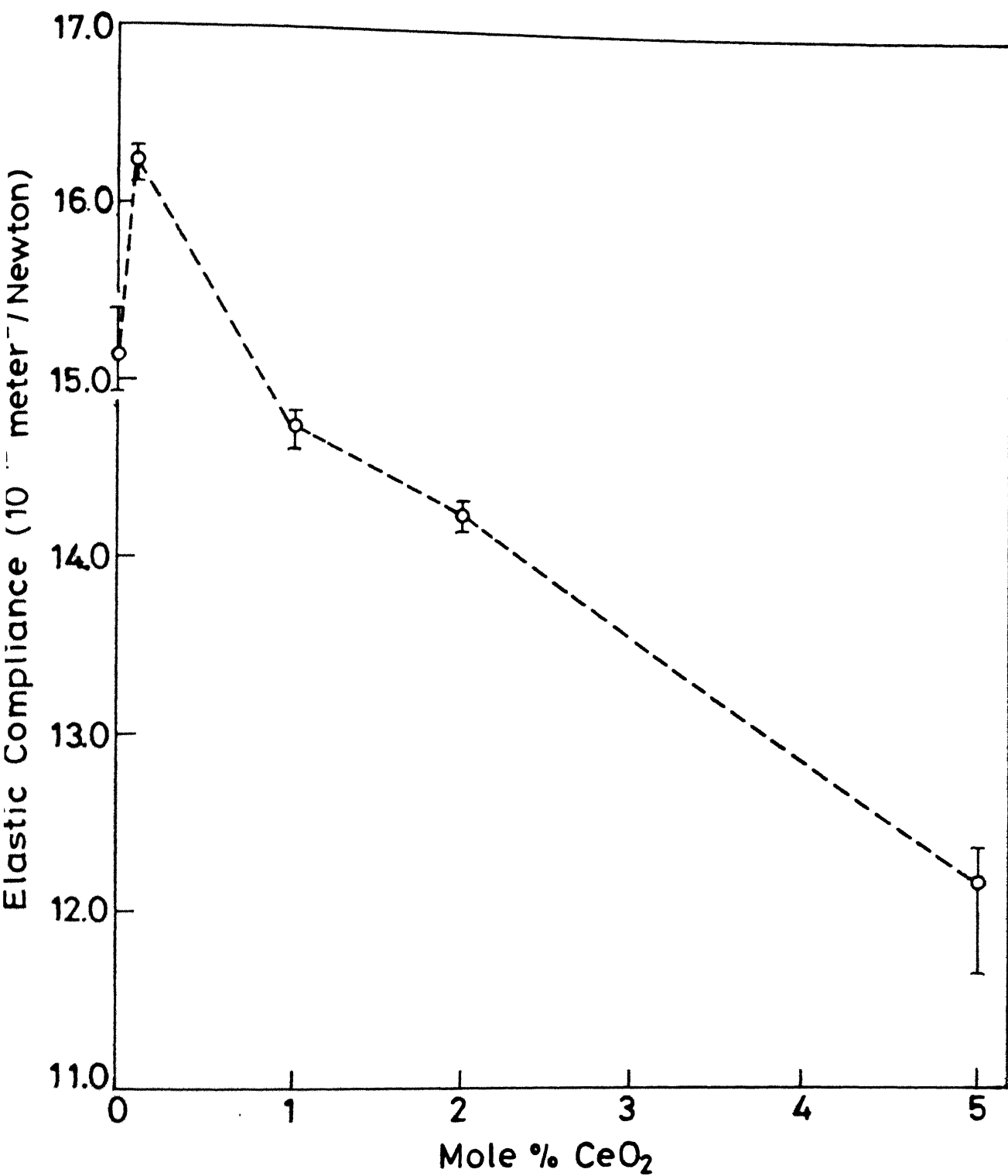


Fig. 3.8 Variation of elastic compliance with concentration of ceria.

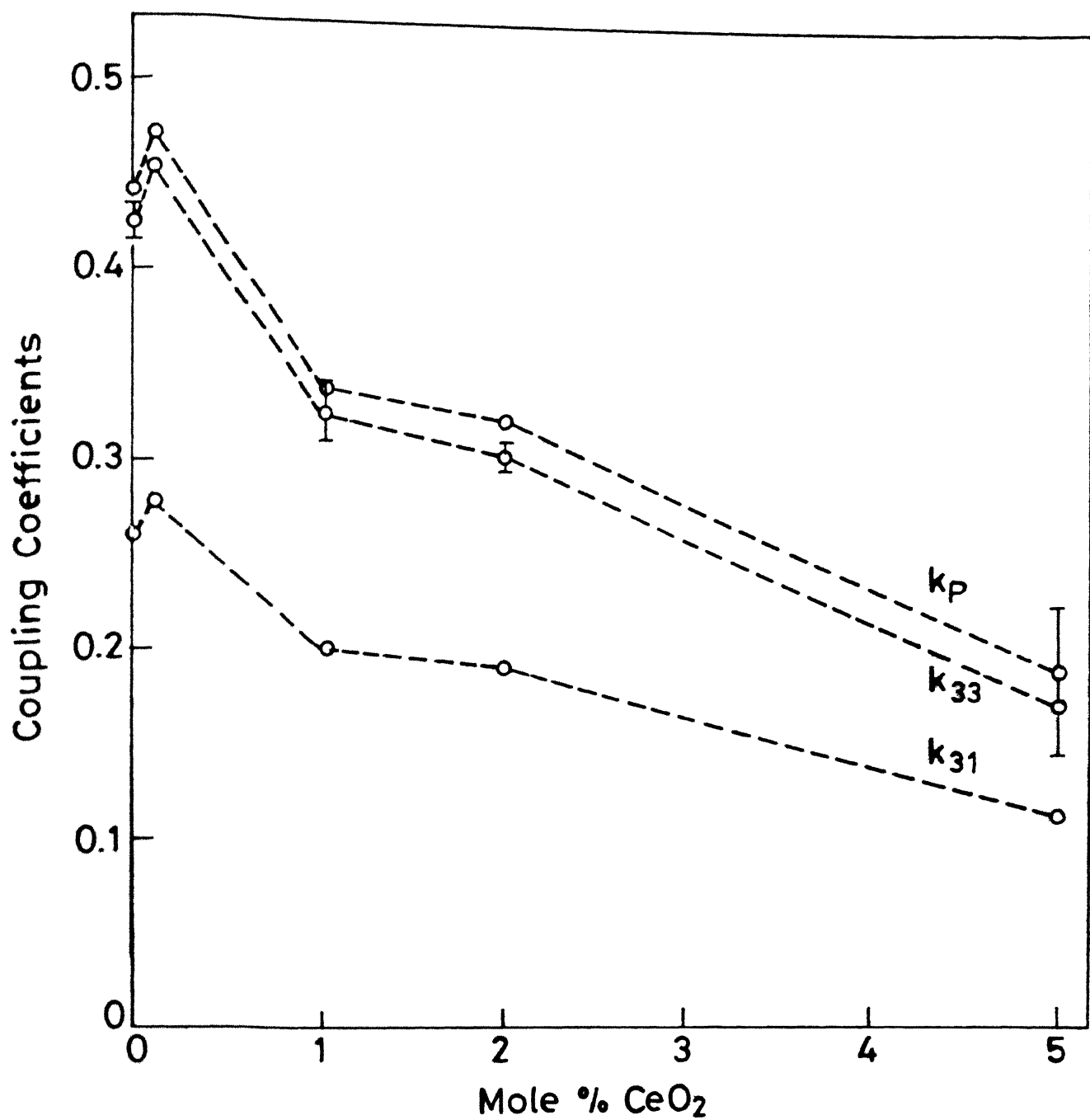


Fig.3.9 Variation of coupling coefficient with concentration of ceria.

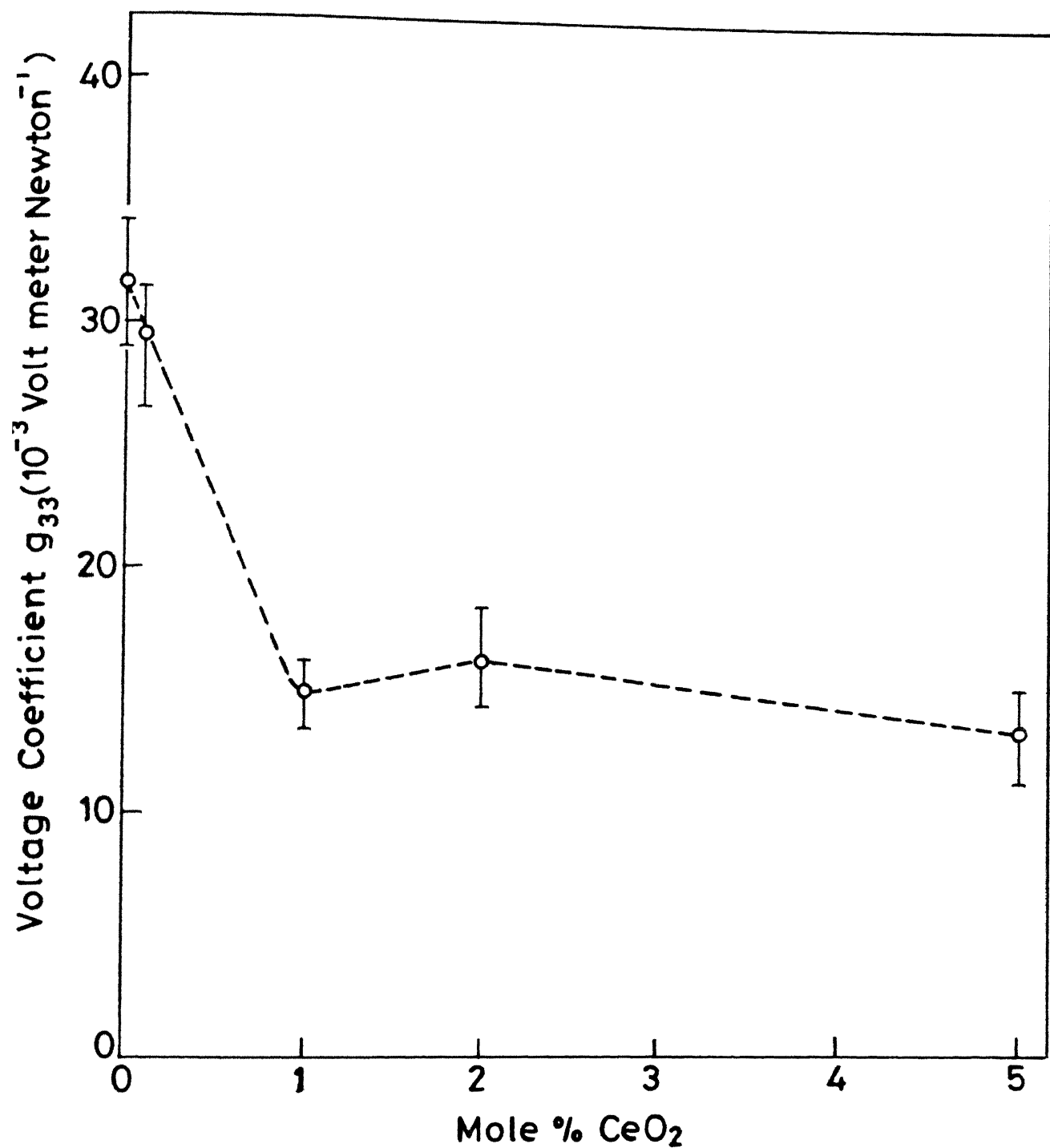


Fig. 3.10 Variation of voltage coefficient with concentration of ceria.

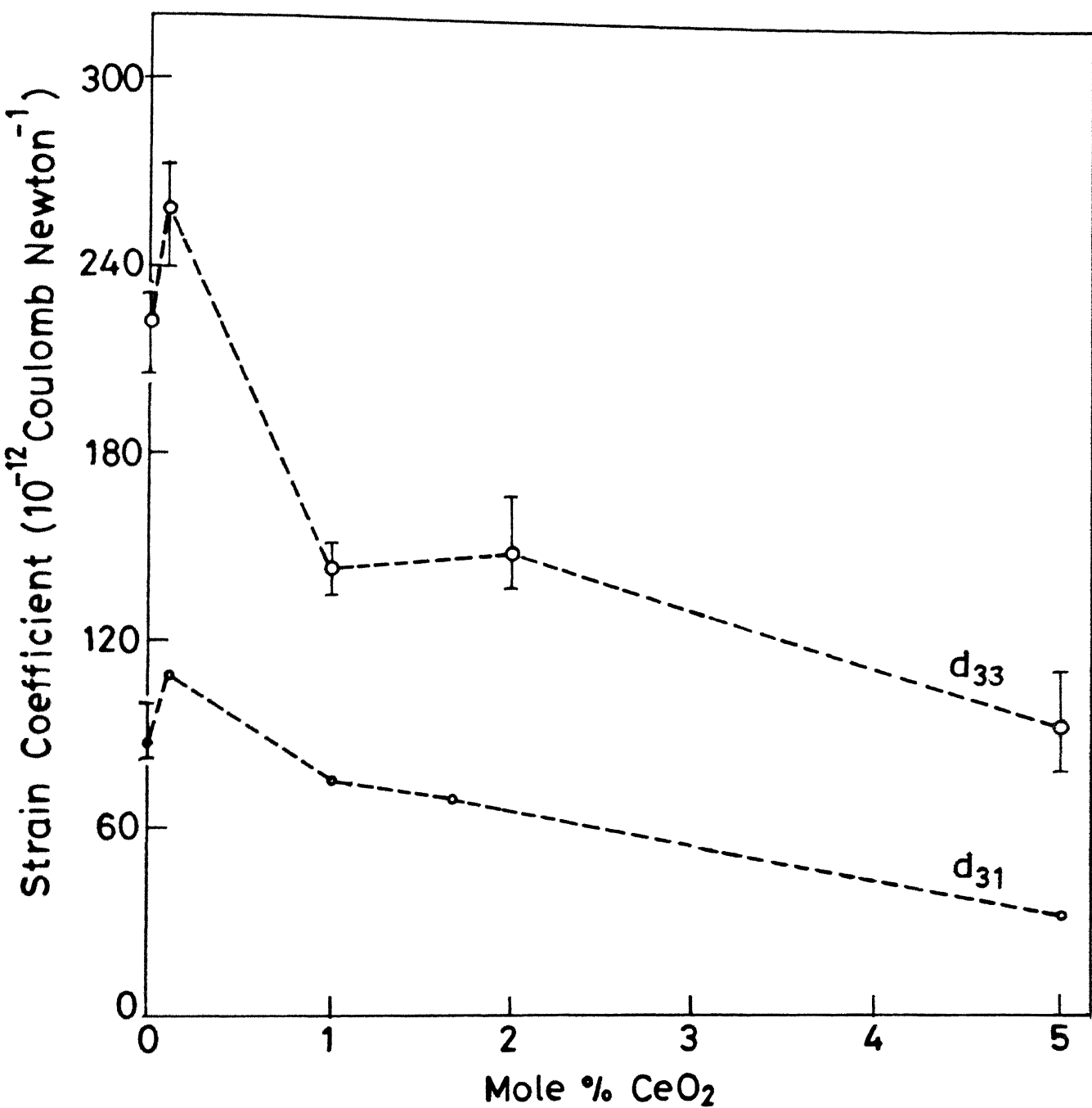


Fig. 3.11 Variation of strain coefficient with concentration of ceria.

rhombohedral edge of the MPB. Thus a maximum in the piezoelectric properties as observed here agrees with the observation of Jaffe et al mentioned earlier.

However, a value of  $d_{33}$  equal to  $280 \times 10^{-12} \text{ C.N}^{-1}$  observed here for 0.1 mole%  $\text{CeO}_2$  is significantly higher than the best values for undoped PZT reported in literature. The latter range from 110 to  $225 \times 10^{-12} \text{ C.N}^{-1}$  depending on the composition, the maximum being obtained near the morphotropic phase boundary. Thus the enhancement in the piezoelectric properties is more than that obtained in PZT with optimum combination of the two phases. This result is of practical interest because  $\text{CeO}_2$  is relatively an inexpensive material, available indigenously in high purity in contrast to other additives like  $\text{Nb}_2\text{O}_5$  etc., which are in short supply.

### 3.4 Mechanical Properties

It is true that the primary properties of interest of the piezoelectric materials are the piezoelectric properties but the mechanical properties may limit the application of a particular material. Mechanical strength of piezoelectric ceramics is a factor that must be considered for design of transducer. Many applications involve electrically or thermally induced stresses as well as possible mechanical loads due to vibration. Further, when fracture of a component does occur the analysis of fractured surface, characterisation of fracture initiating defect lead to the knowledge by which further improvement in material selection,

fabrication modification and changes in design parameters can be achieved to develop a better material.

### 3.4.1 Vickers Hardness

The raw data and the result of Vicker's Hardness are given in table 3.10.

Table 3.10

#### Vickers Hardness of Ceria Doped PZT Ceramics

Concentration of $\text{CeO}_2$ doping (mole %)	Load in kg	Range of diagonal length of indenta- tion -3 (10 mm)	Average diagonal length of indenta- tion -3 (10 mm)	Range of Vicker's hardness ( $\text{kg/mm}^2$ )	Average Vicker's hardness ( $\text{kg/mm}^2$ )
0	2.5	176-207	195.3	108.2-149.6	121.5
0.1	5.0	230-252	241.3	146.0-175.2	159.62
1.0	10.0	305-340	322.2	160.4-199.3	178.6
2.0	10.0	306-323	315.6	177.7-198.0	186.11
5.0	10.0	252-289	265.2	236.5-292.0	263.62

The measurement of Vicker's Hardness shows an steady improvement in the hardness of the PZT material with increasing amount of ceria. Figure 3.12 shows graphically the change of Vicker's hardness with increasing  $\text{CeO}_2$  concentration.

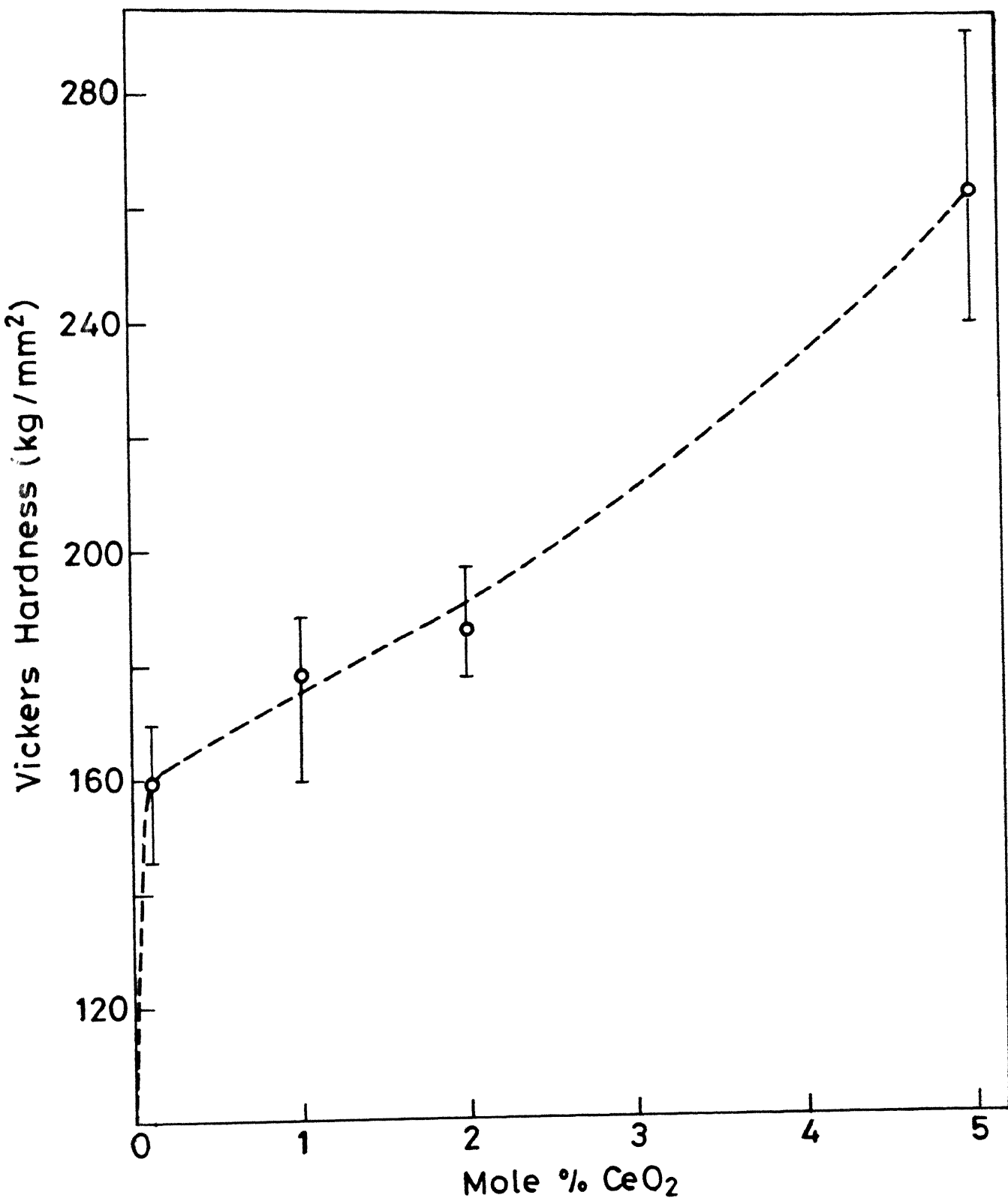


Fig. 3.12 Variation of Vickers hardness with concentration of ceria.



### 3.4.2 Modulus of Rupture

The modulus of rupture value of the ceria doped PZT ceramics are given in Table 3.11

**Table 3.11**  
**MOR of Ceria Doped PZT Ceramics**

Concentration of ceria (mole %)	Range of MOR in MPa	Average value of MOR in MPa
0	45.23-53.83	48.8
0.1	33.78-41.14	36.01
1.0	22.46-30.55	26.71
2.0	24.21-36.6	29.48
5.0	29.12-36.83	33.15

MOR values are graphically represented in figure 3.15. MOR is highest for pure PZT and reaches minimum at the doping level of 1.0 mol percent ceria. Then it again increases but remains less than pure PZT.

### 3.4.3 Young's Modulus

Values of Young's modulus are given in table 3.12

Table 3.12

## Young's Modulus of Ceria Doped PZT Ceramics

Concentration of ceria (mole %)	Range of values of Young's modulus (GPa)	Average value of Young's modulus (GPa)
0	26.71-34.92	30.83
0.1	17.68-29.78	22.78
1.0	18.86-31.21	25.35
2.0	19.60-30.18	26.56
5.0	22.45-37.92	32.14

Variation of Young's modulus with concentration of ceria is graphically represented in figure 3.13. Minimum value of Young's Modulus is obtained at 0.1 mol percent concentration of ceria.

#### 3.4.4 Fracture Toughness ( $K_{IC}$ )

Values of fracture toughness are given in table 3.13 and graphically represented in figure 3.13

Table 3.13

## Fracture Toughness of Ceria Doped PZT Ceramics

Concentration of of ceria (mole %)	Range of Values of $K_{IC}$ (MPa $m^{1/2}$ )	Average Values of $K_{IC}$ (MPa $m^{1/2}$ )
0	1.1828-1.2440	1.219
0.1	0.8041-0.9925	0.9145
1.0	0.6723-0.8377	0.7290
2.0	0.8645-0.9550	0.9082
5.0	0.7735-0.9583	0.8544

$K_{IC}$ , the fracture toughness of a material, is a material property and represents the resistance to unstable crack propagation in a material. It is high if there are many energy dissipating processes occurring during crack propagation. Thus it is a sensitive function of the microstructure of the material. It will also depend on the chemistry and crystal structure of the material.

The following microstructural changes are observed with ceria content (i) the average grain size increases from 3.5 micron to 7.5 micron as the  $CeO_2$  increases for 0 to 5 mole %. (ii) Particles rich in ceria are clearly visible in SEM at 2 mole % ceria. They produce a distinct ceria peak at 5 mole % ceria. It

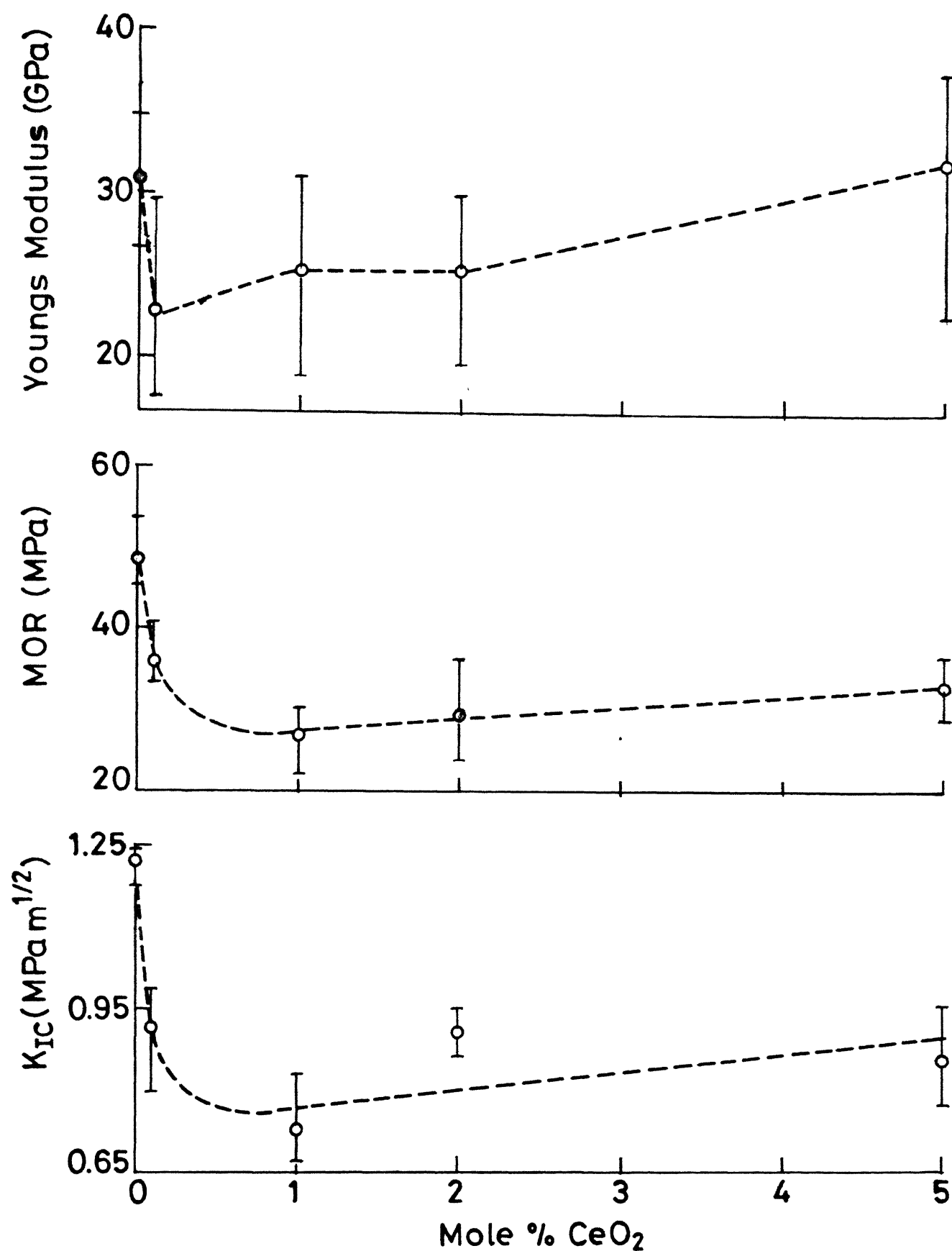


Fig.3.13 Variation of Youngs Modulus, Modulus of Rupture and Fracture Toughness with concentration of ceria.

is possible that they begin to form at lower ceria content, possibly at 1 mole % ceria, but are not observed.

The variation in the  $K_{IC}$  is obviously related to these factors. The dependence of  $K_{IC}$  on grain size is not well understood, conflicting results having been reported. In our results, there is a good correlation between the rise in the  $K_{IC}$  after the minimum and the appearance of the  $CeO_2$  particles. The  $K_{IC}$  begins to increase at the same ceria content at which the ceria particles begin to appear. Second phase particles are known to increase fracture toughness by mechanisms such as crack deflection and microcrack formation. Thus the ceria particles may be responsible for the observed enhancement in the fracture toughness in sample with more than 1.0 mole % ceria.

The relation between the  $K_{IC}$  and the strength,  $\sigma$ , (modulus of rupture) is the following:

$$K_{IC} = \sigma (\pi a)^{1/2}$$

where 'a' is the half crack length. Value of 'a' is related to the size of the flaw such as porosity at which the fracture initiates. Thus a rough order of magnitude estimate of the fracture causing flaw can be obtained from the measured values of  $K_{IC}$  and  $\sigma$ . This gives the following results:

Sample No.	mole % CeO	MOR	K	a
		MPa	MNm <sup>3/2</sup>	(mm)
1	0	48.8	1.219	0.198
2	0.1	36.01	0.9145	0.205
3	1.0	26.71	0.7290	0.237
4	2.0	29.48	0.9082	0.302
5	5.0	33.15	0.8544	0.188

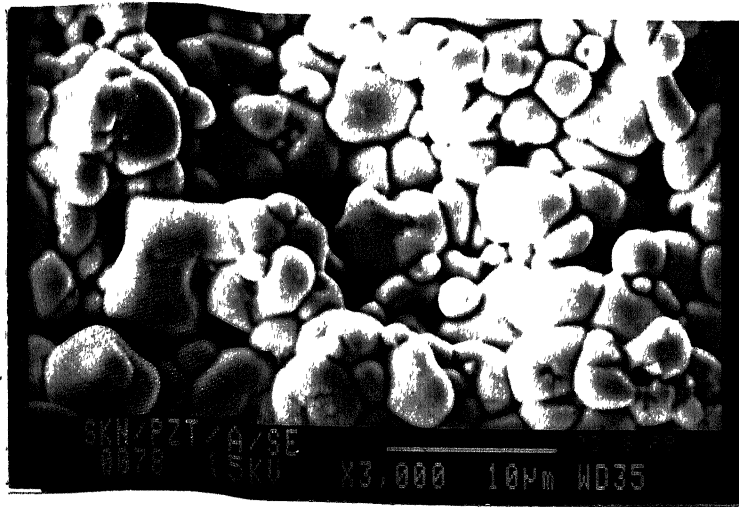
The value of 'a' are nearly constant. Thus the MOR scales directly with  $K_{IC}$ .

In contrast to the other mechanical properties, the hardness continuously increases with increasing ceria content. Vickers Hardness of a material is linked with the resistance of the material to both the elastic and plastic deformation of the surface by indentation. Generally the amount of different phases, residual strain in the lattice, movement of dislocation in the crystal under stress govern the hardness of a material. In this work it has been observed that there is a rise of hardness upto 0.1 mole % CeO<sub>2</sub> and beyond that it rises monotonically with lower slope. This correlates rather well with the decrease in the amount of the rhombohedral phase. Thus 0.1 mole % CeO<sub>2</sub> correspond with edge of rhombohedral phase. Beyond that only tetragonal phase is present. It is also observed that c/a ratio of the tetragonal phase gradually increases with ceria addition.

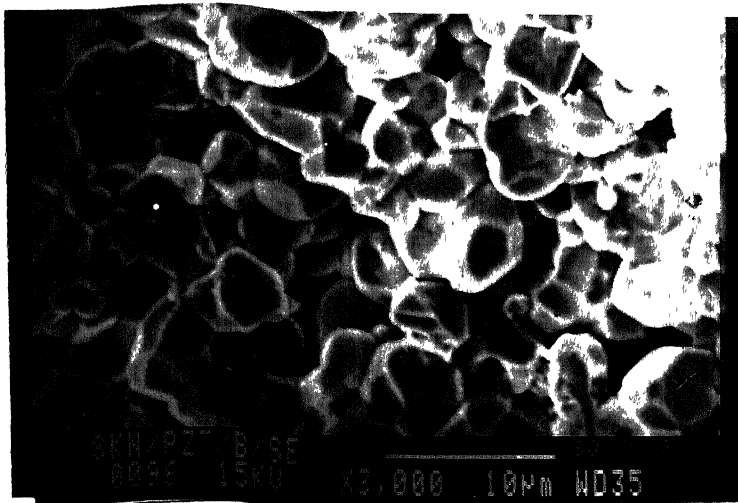
his increasing tetragonality may be responsible for the anolonic increase in the hardness of the tetragonal phase with increases ceria.

## 2.5 Microstructural Analysis

Microstructure of five set of samples are shown here. From the microstructures it is clear that grain size increases gradually with increasing  $\text{CeO}_2$  concentration. The grain size was measured by line intercept method taking 30 grains per set. It varies approximately from 3.5 micron for 0 mole %  $\text{CeO}_2$  to 7.5 micron for 5 mole %  $\text{CeO}_2$  samples. Very small grains of  $\text{CeO}_2$  particles are observed at the 2 mole %  $\text{CeO}_2$  and very clearly at 5 mole %  $\text{CeO}_2$ .

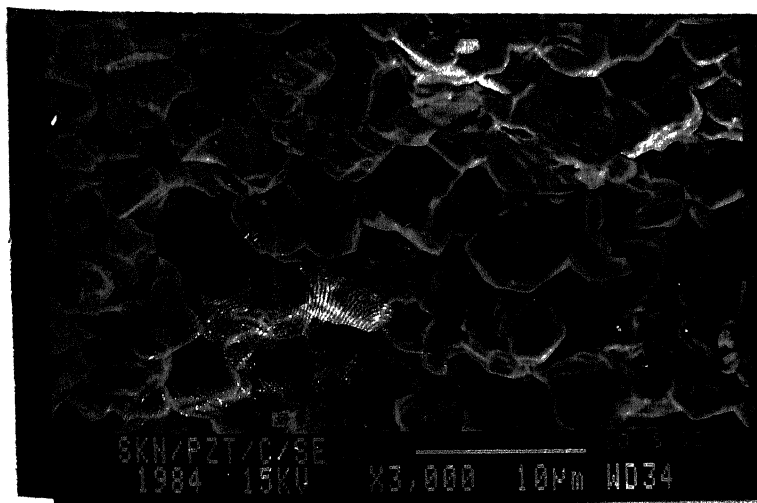


Microstructure of Pure PZT.

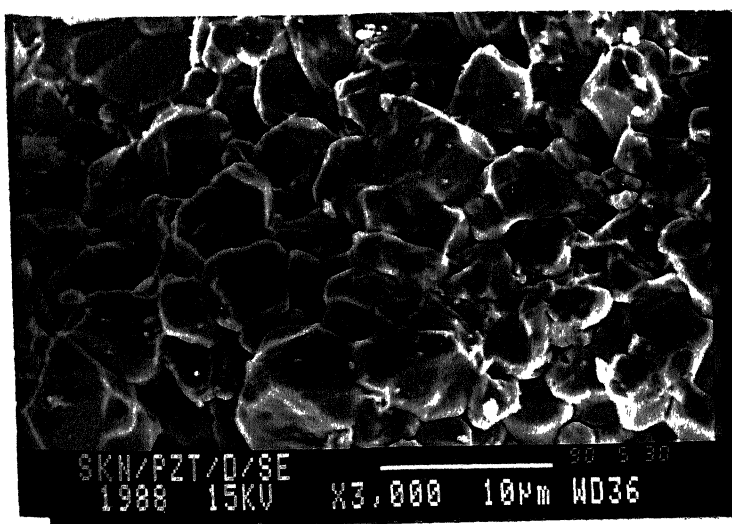


Microstructure of 0.1 mole%  $\text{CeO}_2$  doped PZT

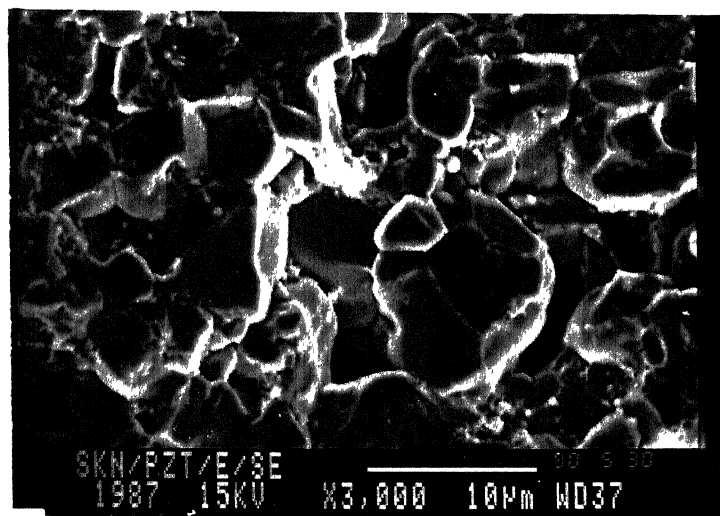




Microstructure of 1.0 mole%  $\text{CeO}_2$  doped PZT



Microstructure of 2.0 mole%  $\text{CeO}_2$  doped PZT



Microstructure of 5.0 mole%  $\text{CeO}_2$  doped PZT

## CHAPTER 4

### CONCLUSIONS AND SCOPE FOR FURTHER WORK

The results obtained by doping ceria in pZT ceramics lead to following conclusions:

(1) Of all the ceria contents investigated (0, 0.1, 1, 2 and 5 mole %), the maximum piezoelectric properties are obtained at 0.1 mole % of ceria.

(2) It has been reported [43] that PZT ceramics doped with 0.6 mole % Thoria shows properties superior to PZT doped with  $\text{Nb}_2\text{O}_5$  or  $\text{La}_2\text{O}_3$ . Thorium and cerium ions are very similar - both

have a valence of 4 and have nearly equal ionic radius. Hence it is possible that  $\text{CeO}_2$  doping in the neighbourhood of 0.6 mole % may also result in improved properties. The range between 0 to 1.0 mole %  $\text{CeO}_2$  should therefore be thoroughly investigated.

(3) At 2 and 5 mole %  $\text{CeO}_2$  microstructure reveals that very fine ceria particles have precipitated at the grain boundaries. It may be worth while to find out the concentration of ceria at which it actually starts to precipitate at the grain boundaries. This will be helpful in explaining the mechanical behaviour of the material.

(4) Mechanical properties of the piezoelectric ceramics are also very important as high stresses are generated during potential and operation as well as during fabrication.

Mechanical fracture of devices is a common occurrence. The observed variation in mechanical properties need to be related to microstructures were carefully to understand the mechanical properties of piezoelectric materials in general.

REFERENCES

1. Cady, W.G.; "Piezoelectricity" Dover Publication Inc. New York, (1964) (Revision of McGraw Hill New York 1946).
2. Mason W.P.; "Piezoelectric Crystals and Their Application to Ultrasonics", Van Nostrand, New York (1950).
3. Jaffe, H.; and Berlincourt D.A.; Proc. IEEE 53, 1372-86 1965.
4. Buchanan, R.C., "Ceramic Materials for Electronics. Processing, Properties and Application", Marcel Dekker, Inc., New York and Basel, 1986.
5. Jaffe, B., Cook, W.R., Jr. and Jaffe, H., "Piezoelectric Ceramics", Academic Press, New York, 1971.
6. Jaffe, B., Roth, R.S. and Marzullo, S.; "Piezoelectric Properties of Lead Zirconate-Lead Titanate Solid Solution Ceramics", J. Appl. Phys. 25, 909-10 1954.
7. Shirane G., Jona, F., and Pepinsky, R.; Proc. I.R.E., 42, 1738 1955.
8. Sawaguchi, E.; "Ferroelectricity Vs. Antiferroelectricity in the Solid Solution of  $\text{PbZrO}_3$  -  $\text{PbTiO}_3$ ", J. Phys. Soc. Japan, 8 615-29 1953.
9. Shirane, G., and Takeda. A.; "Phase Transition in Solid Solutions of  $\text{PbZrO}_3$  and  $\text{PbTiO}_3$  (I) Small Concentration of  $\text{PbTiO}_3$ ", J. Phys. Soc. Japan 7 5-11, 1952.
10. Barnett, H.M.; Evidence for New Phase Boundary in the Ferroelectric Lead Zirconate-Lead Titanate System, J. Appl. Phys. 33 1606 1962.

11. Michel, C., Moreau, J.M., Achenbach, G.D., Gerson, R. and James, W.J.; Solid State Communication 7 865-8 1969.
12. AriGur, P. and Benguigui, L.; "Direct Determination of the Coexistence Region in the Solid Solution  $Pb(Zr_{1-x}Ti_x)_3O_{10}$ " J. Phys. D. 8 1856-62 1975.
13. Mabud, S.A.; "The Morphotropic Phase Boundary in PZT Solid Solution" J. Appl. Crystallography 13[3] 211-16 1960.
14. Matsuo, Y. and Sasaki, H.; "Formation of Lead Zirconate-Lead Titanate Solid Solution" J. Am. Ceram. Soc. 48(6) 289-91 1965.
15. Ohno, T., Takahashi, M. and Tsubouchi, N.; "Perovskite Formation Process in  $Pb(ZrTi)_3O_{10}$  Ceramic containing  $SiO_2$ " J. Jap. Soc. Powder Metall., 20(5) 154-59 1973.
16. Hankey, D.L., and Biggers, J.V.; "Solid-state Reactions in the System  $PbO-TiO_2-ZrO_2$ " J. Am. Ceram. Soc. 64[12] C-172, C-173 1981.
17. Chandratreya, S.S., Fulrath, R.M., and Pask, J.A., "Reaction Mechanisms in the Formation of PZT Solid Solution," J. Am. Ceram. Soc. 64(7) 422-25 1981.
18. Hardtl, K.H., and Rau, H.; "PbO Vapour Pressure in the  $Pb(Ti_{1-x}Zr_x)_3O_{10}$  System" Solid State Communication 7 41-45 1969.
19. Webster, A.H., Weston, T.B., and Bright, Norman F.H.; "Effect of PbO Difficiency on the Piezoelectric

Properties of Lead-Zirconate-Titanate Ceramics J. Am. Ceram. Soc. 50(9) 490-491 1967.

20. Hankey, Dana L. and Biggers, James V.; "Effect of Packing Pressure and Particle Size Variations on the Reaction Kinetics for  $\text{PbTiO}_3$  and  $\text{PbZrO}_3$  Formation" J. Am. Ceram. Soc. 65(5) C-74 & C-75 1982
21. Kakegawa, K., Mohri, J., Takahashi, K., Yamamura, H. and Shirasaki, H.; "A Compositional Fluctuation and Properties of  $\text{Pb}(\text{Zr}, \text{Ti})\text{O}_3$  Solid State Communication 24(11) 769-72 1977.
22. Kakegawa, K., Mohri, J., Ishiguro, H., Takahashi, K. and Shiraski, S.; "Synthesis of  $(\text{Ba}, \text{Pb})\text{TiO}_2$  Solid Solution Having No Composition Fluctuation" Chem. Lett. 1655-58 1982.
23. Kakegawa, K. and Mohri, J.; "Synthesis of  $(\text{Ba}, \text{Pb})(\text{Zr}, \text{Ti})\text{O}_3$  Solid Solution Having No Compositional Fluctuation J. Am. Ceram. Soc. 68(8) C-204 - C-205 1985.
24. Kakegawa, K., Arai, K., Sasaki, Y. and Tomizawa, T.; "Homogeneity and Properties of Lead Zirconate Titanate Prepared by a Combination of Thermal Spray Decomposition Method with Solid-Phase Reaction" J. Am. Ceram. Soc. 71(1) C49-C52 1983.
25. Snow, G.S.; "Improvement in Atmosphere Sintering of Transparent PLZT Ceramics" J. Am. Ceram. Soc. 56[2] 91 1973

26. Snow, G.S.; "Elimination of Porosity in  $\text{Pb}(\text{Zr}, \text{Ti})\text{O}_3$  Ceramics by Liquid Phase Sintering" J. Am. Ceram. Soc. 57(6) 272 1974.
27. Atkin, R.B. and Fulrath, R.M.; "Point Defects and Sintering of Lead Zirconate-Titanate" J. Am. Ceram. Soc. 54(5) 265-70 1971.
28. Holman, R.L. and Fulrath, R.M.; "Intrinsic Nonstoichiometry in Single Phase  $\text{Pb}(\text{Zr}_{0.5}\text{Ti}_{0.5})\text{O}_3$ " J. Am. Ceram. Soc. 55(4) 192-97 1972.
29. Holman, R.L. and Fulrath, R.M.; "Intrinsic Nonstoichiometry in the Lead-Zirconate, Lead-Titanate System Determined by Knudsen Effusion" J. Appl. Phys. 44(12) 5227-36 1973.
30. Kingon, Angus I. and Clark J. Brain; "Sintering of PZT Ceramics : I, Atmosphere Control" J. Am. Ceram. Soc. 66(4) 253-56 1983.
31. Kingon, Angus I. and Clark J. Brain; "Sintering of PZT Ceramics : II, Effect of  $\text{PbO}$  Content on Densification Kinetics" J. Am. Ceram. Soc. 66(8) 256-260 1983.
32. Buckner, D.A. and Wilcox, P.D.; "Effect of Calcining on Sintering of Lead Zirconate-Titanate Ceramics" Am. Ceram. Soc. Bull. 51(3) 218-22 1972.
33. Hall, C.E. and Blum, J.B.; "Effect of Sintering Rate on the Electrical Properties of Sr-PZT" Ferroelectrics 37 643-646 1981.



34. Baumgartener, Charles E.; "Fast Firing and Conventional Sintering of Lead Zirconate Titanate Ceramic" J. Am. Ceram. Soc. 71(7) C350-C353 1988.
35. Okazaki Kiyoshi; "Developments in Fabrication of Piezoelectric Ceramics" Ferroelectrics 41 77-96 1982.
36. Hardt, K.H. and Hennings, D.; "Distribution of A-site and B-site Vacancies in  $(\text{Pb,Lu})(\text{Ti,Zr})\text{O}_3$  Ceramics" J. Am. Ceram. Soc. 55(5) 230-231 1972.
37. Hennings Detlev; "Range of Existence of Perovskite Phases in the System  $\text{PbO-TiO}_2\text{-La}_2\text{O}_3$ " Mater. Res. Bull. 6[5] 329-39 1971.
38. Gonnard, P. and Troccaz, M.; "Dopant Distribution Between 'A' and 'B' Sites in the PZT Ceramics of Type  $\text{ABO}_3$ " Journal of Solid State Chemistry 23 321-326 1978.
39. Roy Chowdhury, P. and Deshpande, S.B. ; "Piezoelectric Properties of Ferroelectric  $\text{Pb}(\text{Zr,Ti,Sn})\text{O}_3$  Ceramics Modified with 3 & 5-Valent Materials" Indian Journal of Pure & Applied Physics 15 395-399 1977.
40. Kulcsar, Frank; "Electromechanical Properties of Lead Titanate Zirconate Ceramics Modified with Certain Three-or Five-Valent Additions" J. Am. Ceram. Soc. 42(7) 343-49 1959.
41. Takahashi, S. and Takahashi, M.; "Effects of Impurities on the Mechanical Quality Factor of Lead Zirconate Titanate Ceramics" Japanese J. Appl. Phys. 11(1) 31-35 1972.

42. Frank, Kulscar; "Electromechanical Properties of Lead Titanate Zirconate Ceramics with Lead Partially Replaced by Calcium or Strontium" J. Am. Ceram. Soc. 42 49-51 1959.
43. Frank, Kulscar; "Electromechanical Properties of Lead Titanate Zirconate Ceramics Modified with Tungsten and Thorium" J. Am. Ceram. Soc. 48 59 1965.
44. Cullity, B.D. "Elements of X-ray Diffraction" Addison Wesley Publishing Company, Inc. NewYork, Second Edition 1978.
45. Jaffe, H. and Berlincourt, D.A. "Piezoelectric Transducers Materials" Proc. IEEE 53(10) 1372-86 1965.
46. Baerwald, H.G. "Thermodynamic Theory of Ferroelectric Ceramics" Phy. Rev. 105 480-86 1957.
47. Redin, R., Marks, G. and Antoniak, C.; "Symmetry Limitations to Polarization of Polycrystalline Ferroelectrics" J. Appl. Phys. 34 600 1963.
48. Cherry, W.L. Jr. and Alder, R.; "Piezoelectric Effect in Polycrystalline Barium-Titanate" Phy. Rev. 72 981-82 1947.
49. Belding, J.H. and McLaren, M.G. "Behaviour of Modified Lead Zirconate-Lead Titanate Piezoelectric Ceramics Under High Electric Fields" Am. Ceram. Soc. Bull. 49 1025 1970.
50. Gerson, R. and Marshall, T.C. "Effect of Porosity and Sample Thickness on Breakdown in  $Pb(TiZr)O_3$  Ceramics" J. Appl. Phys. 30 1650-53 1959.

51. "IRE Standards of Piezoelectric Crystals: Measurements of Piezoelectric Ceramics" PROC. IRE 49 1161-69 1961.
52. Mason, W.P. "Electrostrictive Effect in Barium Titanate Ceramics" Phy. Rev. 105 480-86 1957.
53. Dieter, G.E. "Mechanical Metallurgy" McGraw Hill Book Company 1986.
54. 1984 Annual Book of ASTM Standard, Section : Metals Test Methods and Analytical Procedures . Vol. 03.01 : Metals-Mechanical Testing, Elevated and Low Temperature Tests, Designation E885-84.
55. Jones, Robin L. and Rowcliffe, David J.; "Use of Notched Bend Beams to Measure the Toughness of Ceramics" Am. Ceram. Soc. Bull. 58(12) 1195 1979.
56. Isupov, V.A.; "Dielectric Polarisation of  $\text{PbTiO}_3$  -  $\text{PbZrO}_3$  Solid Solutions" Sov. Phys. Solid St. 12(5) 1084-88 1970.
57. Saley, V.S., Ponomarev, Ju. A., Kumov, V.V. and Poplavko, Yu. M.; "X-ray Study of PZT Solid Solutions in the Tetragonal-Rhombohedral Phase Transition Composition Area" Ferroelectrics 22 805 1978
58. Lucuta, P.G., Constantinescu, F.L. and Barab, D.; "Structural Dependence of Lead Zirconate Titanate Solid Solutions" J. Am. Ceram. Soc. 68(10) 533-37 1985.
59. Isupov, V.A.; In : Dielectriki poluprovodniki (Kiev, 1978, 13) p. 14.
60. Isupov, V.A.; Fiz. tverdogo tela. 22 172 1980.

61. Dorofeeva, V.V., Saley, V.S. and Didkovskaya, O.S.;  
Neorganicheskie materialy, 16 2043 1980.
62. Chiang, S.S., Fulrath, R.M. and Pask, J.A.; "Influence of  
Microcracking and Slow Crack Growth on the Planar Coupling  
Coefficient in PZT" J. Am. Ceram. Soc. 64[10] C141-C143  
1981.
63. Chung, H.T. and Kim, H.G., "Characteristics of Domain in  
Tetragonal Phase PZT Ceramics" Ferroelectrics 76 327-33  
1987.
64. Chung Hum-Taeg, Shin Byoung-Chul and Kim Ho-Gi; "Grain  
Size Dependence of Electrically Induced Microcracking in  
Ferroelectric Ceramics" J. Am. Ceram. Soc. 72(2) 327-29  
1989.
65. Muller, O. and Roy, R., "Crystal Chemistry of Nonmetallic  
Materials" Springer-Verlag, New York 1974.

## APPENDIX 1

## Measurement scheme for piezoelectric ceramics

Constants	Specimen and orientation	Measurement scheme, or calculation method
$\epsilon_{11}^p, k_{31}, d_{31}$	Bar plated on faces perpendicular to $Z$ .	Resonance measurements of the length extensional mode.
$s_{11}^p$	Bar plated on faces perpendicular to $Z$ .	From above, using $s_{11}^p = (1 - k_{31}^2)s_{11}^f$ .
$\epsilon_{33}^p$	Bar plated on faces perpendicular to $Z$ .	Measurement of low-frequency capacitance.
$s_{33}^p$	Bar poled along $Z$ , but with plating on faces perpendicular to $X$ .	Overtone of thickness shear mode of the same bar as above, but with signal field along $X$ .
$\epsilon_{11}^f$	Bar poled along $Z$ , but with plating on faces perpendicular to $X$ .	Measurement of low-frequency capacitance.
$\epsilon_{11}^f$	Bar poled along $Z$ , but with plating on faces perpendicular to $X$ .	Measurement of high-frequency (clamped) capacitance.
$k_{15}$	Bar poled along $Z$ , but with plating on faces perpendicular to $X$ .	$k_{15}^2 = 1 - \epsilon_{11}^f/\epsilon_{11}^p$ .
$s_{33}^p$	Bar poled along $Z$ , but with plating on faces perpendicular to $X$ .	$s_{33}^p = s_{33}^f/(1 - k_{15}^2)$ .
$s_{11}^f, s_{12}^f$	Square plate with faces perpendicular to $Z$ .	Fundamental resonance frequencies of the two contour-extensional modes of a square plate.
$s_{12}^f$	Square plate with faces perpendicular to $Z$ .	$s_{12}^f = s_{12}^f - k_{31}^2 s_{11}^f$ .
$s_{33}^p, d_{33}, k_{33}$	Bar plated on faces perpendicular to $Z$ , and with length along $Z$ .	Resonance measurements of length extensional mode.
$s_{33}^p$	Bar plated on faces perpendicular to $Z$ , and with length along $Z$ .	$s_{33}^p = s_{33}^f/(1 - k_{33}^2)$ .
$\epsilon_{11}^f, k_p, d_{31}$	Disk with faces perpendicular to $Z$ .	Resonance measurements of planar extensional mode.
$k_p$	Disk with faces perpendicular to $Z$ .	Resonance measurements of thickness extensional mode.
$d_{31}$	Disk with faces perpendicular to $Z$ .	Measurement of response to hydrostatic pressure.
$d_{33}$	Disk with faces perpendicular to $Z$ .	$d_{33} = d_{31} - 2d_{31}$ .
$\epsilon_{33}^p$	Disk with faces perpendicular to $Z$ .	Overtone $f_p$ of thickness extensional mode.
$s_{11}^p$	Calculation.	Calculated from $\epsilon_{33}^p, s_{12}^p, s_{11}^p$ and $s_{33}^p$ .
$s_{12}^p$	Calculation.	$s_{12}^p = s_{12}^p + d_{31}d_{33}/\epsilon_{33}^p$ .
$\epsilon_{33}^f$	Calculation.	$\epsilon_{33}^f = \epsilon_{33}^p \left[ 1 - \frac{k_p^2 + k_{33}^2 + 2Ak_p k_{33}}{1 - A^2} \right]$ ,
		where
or		$A = \frac{\sqrt{2}s_{12}^p}}{\sqrt{s_{11}^p(s_{11}^p + s_{12}^p)}}$
	Plate with faces perpendicular to $Z$ .	Measurement of high-frequency (clamped) capacitance.

Note:  $s_{12}$ ,  $s_{13}$  and  $d_{31}$  are generally negative.  $k_p$  is taken to be positive when  $d_{31}$  is negative.